Size effect and anisotropy in a transversely isotropic rock under compressive conditions

Kaihui Li[1], Zhen-Yu Yin[2], Dongya Han[1,*], Xiang Fan[3], Rihong Cao[1], Hang Lin[1]

Affiliations:

1. School of Resources and Safety Engineering, Central South University, Changsha 410083, China;

2. Department of Civil and Environmental Engineering, The Hong Kong Polytechnic University, Hong Kong, China;

3. School of Highway, Chang'an University, Xi'an 710064, China.

[*] Corresponding author.

E-mail address: dongya.han@connect.polyu.hk (Dongya Han)

Abstract

A series of uniaxial and triaxial compression tests were performed on slate samples with different diameters at different foliation orientations with respect to the direction of the major principal stress. The size effect and anisotropy in slate, as a transversely isotropic rock, were investigated, and the research focused on aspects of elastic properties, uniaxial compressive strength (*UCS*), triaxial compressive strength (*TCS*), and triaxial residual strength (*TRS*). In the five elastic constants for slate, only the Young's modulus parallel to the isotropic plane is size dependent. The *UCS* follows a descending size-effect model developed from coal. The size-effect behaviors of the *UCS* and *TCS* are similar. Two size-dependent failure criteria are proposed by incorporating the size-effect model for *UCS* into the modified Hoek-Brown and Saeidi failure criteria and are verified against experimental data. This is the first time that the relationship among the compressive strength, specimen size, foliation orientation and confining pressure has been comprehensively captured for transversely isotropic rock. Without an evident size effect, the anisotropic *TRS* has also been effectively captured by a modified cohesion loss model, and two bound equations for the brittleness index are finally proposed for transversely isotropic rock. This work promises to provide an upscaling method for determining the mechanical parameters of transversely isotropic rocks in practical engineering.

Keywords: transversely isotropic rock; compressive test; size effect; anisotropy; failure criterion

List of symbols

A	a constant in the cosine relation
A_0, A_M	A constants for specimen size approaching zero and infinite, respectively
a	a Hoek–Brown parameter
a_{ij}	compliance matrix
B	a material constant in Size Effect Law
D	a constant in the cosine relation
D_0, D_M	D constants for specimen size approaching zero and infinite, respectively

d	specimen diameter
d_0	maximum aggregate size
d_f	fractal dimension
E , E'	elastic moduli parallel to and perpendicular to the plane of transverse isotropy
f_t	strength of a specimen with an infinitesimal size
G'	shear modulus normal to the transversely isotropic plane
g	a constant in the modified cohesion loss model
H	sample height
k	a material parameter in the statistical size-effect model
k_β	a parameter describing the anisotropy effect
m , m_i	a Hoek–Brown parameter
P, Q	material constants in Rafiai's failure criterion
R_c	degree of anisotropy
s	a Hoek–Brown parameter
w	an anisotropy classification index
x, y, z	global co-ordinate system
x', y', z'	local co-ordinate system
α_β	reduction factor of strength associated with the rock anisotropy
β	anisotropic angle
$\beta_{\min}$	angle at which the strength is minimum
γ_{xy} , γ_{yz} , γ_{zx}	shear strain components
ε_x , ε_y , ε_z	axial strain components
λ	a material constant in Size Effect Law
λ_i	a dimensionless parameter in the cohesion loss model for isotropic rocks
λ_0 , λ_m , λ_β	parameters in the modified cohesion loss model for transversely isotropic rocks
ν , ν'	Poisson's ratios parallel to and normal to the transverse isotropic plane

σ_0	strength of a specimen with an infinitesimal size
σ_1, σ_3	maximum and minimum principal stresses
σ_c, σ_{ci}	uniaxial compressive strength of intact rock
σ_{c50}	uniaxial compressive strength obtained from a specimen 50 mm in diameter
σ_d	uniaxial compressive strength of the specimen with a diameter of d
$\sigma_{c\beta}$, σ_β	uniaxial compressive strength at β
$\sigma_{c\beta d}$	uniaxial compressive strength of specimen with d at β
$\sigma_{c(90)}$	compressive strength at β of 90°
$\sigma_{c(\min)}$	minimum compressive strength
σ_M	compressive strength when d approaches infinite
σ_p	peak strength
σ_r	residual strength
σ_t^m	measured tensile strength by experiment
σ_t^{p1}, σ_t^{p2}	tensile strength predicted by the size-dependent modified Hoek-Brown and Saeidi failure criteria
σ_x, σ_y, σ_z	normal stress components
τ_{xy}, τ_{yz}, τ_{zx}	shear stress components
φ	friction angle along the foliation plane
χ	a reduction factor of strength indicating the fracture degree of the rock mass

Abbreviations

BI	brittleness index
MFSL	multifractal scaling law
SD	standard deviation
SEL	size-effect law
TCS	triaxial compressive strength
TRS	triaxial residual strength
UCS	uniaxial compressive strength

USEL unified size-effect law

1. Introduction

The size effect is an important characteristic in brittle and semibrittle materials, e.g., rock and concrete (Aubertin et al. 2000; Masoumi et al. 2016b), and the term refers to the influence of the sample size on measured mechanical properties (Masoumi 2013). Although large-scale in-situ tests can accurately estimate the strength and deformation properties of the surrounding rocks or rock masses of underground structures (e.g., tunnels, caverns and mining stopes), they are not always practical or economical when the difficulty of performing such tests, the time needed and the economic cost are taken into consideration (Tutluoğlu et al. 2015). One of the most promising alternative methods is to scale down the strength and elasticity properties of intact rocks tested in the laboratory to match those of rocks or rock masses in practical engineering (Li et al. 2018; Wilson 1983). At this point, a proper size-effect model is essential.

There have been many investigations into the size effect in intact rocks under different stress conditions, including uniaxial compressive testing (Darbor et al. 2019; Darlington et al. 2011; Elkadi et al. 2006; Hawkins 1998; Hoek and Brown 1980; Masoumi et al. 2015; Nishimatsu et al. 1969; Pierce et al. 2009; Quiñones et al. 2017; Thuro et al. 2001; Yoshinaka et al. 2008; Zhai et al. 2020; Zhang et al. 2011), indirect tensile testing (Bažant 1997; Carpinteri et al. 1995; Chen et al. 2021; Elkadi et al. 2006; Masoumi et al. 2018; Masoumi et al. 2015; Masoumi et al. 2017; Rocco et al. 1999a; Rocco et al. 1999b; Thuro et al. 2001), point loading testing (Broch and Franklin 1972; Hawkins 1998; Masoumi 2013; Masoumi et al. 2018; Thuro and Plinninger 2001) and triaxial compressive testing (Aubertin et al. 2000; Hoek and Brown 1980; Masoumi et al. 2016b; Medhurst and Brown 1998). Four classical types of size-effect models were reviewed extensively by Masoumi et al. (2015) and have been established based on the theories of statistics (Weibull 1951), fracture energy (Bažant 1984), multifractality (Carpinteri et al. 1995), and mixed fractals with fracture energy (Bažant 1997). Moreover, Masoumi et al. (2015) presented another size-effect model, viz., the unified size-effect law (USEL), which captures both the ascending and descending uniaxial compressive strength (UCS) trends of six rock types. Nevertheless, the aforementioned size-effect models are all deduced from isotropic media, neglecting the influence of anisotropy. In fact, natural rocks are more or less anisotropic. The anisotropy in rocks is reflected by the different physical and mechanical properties in different directions (Li et al. 2020b). Typical anisotropic rocks include sedimentary and metamorphic rocks, e.g., shale, siltstone, claystone, slate, phyllite and schist. Due to their stratified or foliated structures, such rocks can further be regarded as transversely isotropic materials, in which one privileged direction exists and the material behavior has rotational symmetry with regard to that direction (Amadei 1996; Pei 2008). Although the Earth's crust is composed of approximately 95% igneous rocks and 5% sedimentary and metamorphic rocks, sedimentary and metamorphic rocks make up approximately 75% of the Earth's surface (Wittke 2014). Accordingly, transversely isotropic rocks are widely encountered in civil, mining, petroleum, geothermal and radioactive waste disposal engineering (Chiarelli et al. 2003; Corkum and Martin 2007; Han et al. 2020a,b; Ma et al. 2018; Meier et al. 2015; Zheng et al. 2019). Therefore, investigating the size effect in transversely isotropic rock is an imperative task for rock engineering practitioners.

Recently, based on the descending size-effect trend and the strength anisotropy, a universal equation describing the relationship among the anisotropic angle, sample size and UCS was proposed by Song et al. (2018) for coal, which can be modeled as an orthotropic material (Amadei 1996). This equation also promises to be extended for transversely isotropic rock. Furthermore, Li et al. (2020a) found that the indirect tensile strength of slate is closely related to the loading-foliation angle and specimen size, which displays an ascending and then descending size-effect trend when the loading-foliation angle is low (0°-30°), whereas it presents a descending size-effect trend when the loading-foliation angle is in the medium to high range (45°-90°). Finally, a unified size-effect relation including two equations was proposed and verified against the experimental data to capture the ascending and descending size-effect trends and the relationship among the indirect tensile strength, specimen size and loading-foliation angle. However, to date, there has been no study involving the size effect in transversely isotropic rocks under triaxial conditions.

In this study, the elastic and strength parameters of slate samples are measured by compression tests and then the Hoek-Brown, Saeidi failure criteria and the cohesion loss model are modified to capture the anisotropy and size effect on the compressive strength of slate rocks. The results may provide an upscaling method for determining the mechanical parameters of transversely isotropic rocks, leading to a more reliable design for rock engineering, such as enhanced geothermal systems and nuclear waste repositories. The paper is divided into five sections, the remainder of which is organized as follows. Section 2 provides a theoretical background for the determination of the elastic constants of transversely isotropic rocks and size-effect models in relation to triaxial tests. Section 3 shows the sample preparation and testing setup for compression tests, with the results and discussion further elucidated in Section 4. Finally, conclusions are drawn in Section 5.

2. Theoretical background

2.1 Determination of the elastic constants for transversely isotropic rocks

As seen in Fig. 1, the cylinder of a transversely isotropic material under compression has a height of H and a diameter of d. The global coordinate system (x, y, z) is rotated counterclockwise with an angle of $(\pi/2-\beta)$ relative to the local coordinate system (x', y', z'). β is the orientation of foliation with respect to the direction of the major principal stress. The local system is affiliated with the plane of transversely isotropy, with the x'-axis and the y'-axis parallel to and normal to the plane of transverse isotropy, respectively, and the z'-axis coincides with the z-axis. According to the generalized Hooke's Law, the constitutive model of transversely isotropic media is expressed in global coordinates as follows:

$$\begin{Bmatrix} \varepsilon_x \\ \varepsilon_y \\ \varepsilon_z \\ \gamma_{yz} \\ \gamma_{zx} \\ \gamma_{xy} \end{Bmatrix} = \begin{bmatrix} a_{11} & a_{12} & a_{13} & a_{14} & a_{15} & a_{16} \\ a_{21} & a_{22} & a_{23} & a_{24} & a_{25} & a_{26} \\ a_{31} & a_{32} & a_{33} & a_{34} & a_{35} & a_{36} \\ a_{41} & a_{42} & a_{43} & a_{44} & a_{45} & a_{46} \\ a_{51} & a_{52} & a_{53} & a_{54} & a_{55} & a_{56} \\ a_{61} & a_{62} & a_{63} & a_{64} & a_{65} & a_{66} \end{bmatrix} \begin{Bmatrix} \sigma_x \\ \sigma_y \\ \sigma_z \\ \tau_{yz} \\ \tau_{zx} \\ \tau_{xy} \end{Bmatrix} \tag{1}$$

After postulating the medium in the direction along the transversely isotropic plane to be linearly elastic, homogeneous and continuous, Amadei (2012) deduced the expressions of a_{ij}. The three components of a_{ij} utilized in uniaxial compressive conditions to determine the five independent elastic constants for transversely isotropic rocks are provided as follows:

$$\begin{aligned} a_{12} &= \frac{\varepsilon_x}{\sigma_y} = \frac{\sin^2 2\beta}{4}\left(\frac{1}{E} + \frac{1}{E'} - \frac{1}{G'}\right) - \frac{\nu'}{E'}(\sin^4\beta + \cos^4\beta) \\ a_{22} &= \frac{\varepsilon_y}{\sigma_y} = \frac{\sin^4\beta}{E'} + \frac{\cos^4\beta}{E} + \frac{\sin^2 2\beta}{4}\left(\frac{1}{G'} - \frac{2\nu'}{E'}\right) \\ a_{32} &= \frac{\varepsilon_z}{\sigma_y} = -\cos^2\beta\frac{\nu}{E} - \sin^2\beta\frac{\nu'}{E'} \end{aligned} \tag{2}$$

where E and E' denote the elastic moduli parallel and perpendicular to the transversely isotropic plane, respectively; ν and ν' represent the Poisson's ratios parallel and normal to the transversely isotropic plane, respectively; and G' is the shear modulus in the direction normal to the transversely isotropic plane.

The most frequently-used method for determining the five elastic constants for transversely isotropic rocks under uniaxial compression tests was presented by Amadei (1996) and Cho et al. (2012). In this method, at least two specimens (e.g., prismatic and cylindrical) with different foliation orientations (β) are required, provided that one of them is inclined relative to the isotropic plane (0°<β<90°). Fig. 2 shows the arrangement of biaxial strain gauges for specimens with three different foliation orientations. For each specimen, the two biaxial strain gauges are mounted at the middle of the specimen with axial gauges (No. 1 and 2) parallel to the cylinder axis (y-axis). Circumferential gauges are glued diametrically perpendicular to the axial gauges with each position either in the direction of the dip (No. 3) or the strike (No. 4) of foliation. Substituting the observed stress and strain data from testing into Eq. (1), the obtained equations can be summarized into a matrix containing only unknowns E, E', ν, ν' and G'. After that, the five elastic constants are determined through the method of least squares. Despite the fact that, in theory, a minimum of five independent strain measurements is sufficient for the determination of elastic constants for transversely isotropic rocks, the results of Cho et al. (2012) showed that more strain measurements can improve the prediction accuracy.

2.2 Size-effect models in relation to triaxial tests

Since the Hoek–Brown criterion (Hoek and Brown 1980) is the most well-known, trusted and commonly used triaxial criterion in rock mechanics and rock engineering (Benz et al. 2008; Rafiai 2011), it has been selected as a basic step for deducing the size-effect models applicable in triaxial conditions. The generalized Hoek–Brown failure criterion for rock masses is expressed by

$$\sigma_1 = \sigma_3 + \sigma_{ci}\left(m\frac{\sigma_3}{\sigma_{ci}} + s\right)^a \tag{3}$$

where σ_1 and σ_3 are the maximum (peak strength) and minimum (confining pressure) principal stresses, respectively; σ_{ci} is the UCS of intact rock; and m, s and a are material constants. For intact rocks, $s = 1$ and $a = 0.5$.

The first notable size-effect model considering triaxial confinement was developed by Hoek and Brown (1980), who introduced a statistical descending size-effect model for the well-known Hoek-Brown failure criterion according to

$$\sigma_1 = \sigma_3 + \sigma_{c50}\left(\frac{50}{d}\right)^{0.18}\left(m\frac{\sigma_3}{\sigma_{c50}\left(\frac{50}{d}\right)^{0.18}} + 1\right)^{0.5} \tag{4}$$

where σ_{c50} denotes the UCS obtained from a specimen 50 mm in diameter and d is the sample diameter. Afterward, Medhurst and Brown (1998) succeeded in applying the Hoek-Brown size-effect model to estimate the compressive strength of coal specimens with diameters of 61, 101, 146 and 300 mm at confining pressures in the range of 0-10 MPa.

Subsequently, Masoumi et al. (2016b) observed that both the UCS and the TCS of Gosford sandstone samples with diameters of 25, 50 and 96 mm followed an ascending and then descending size-effect trend. They incorporated the USEL (Masoumi et al. 2015) into the original Hoek-Brown failure criterion according to

$$\sigma_1=\sigma_3+\min\left(\frac{\sigma_0 d^{(d_f-1)/2}}{\sqrt{1+(d/\lambda d_0)}},\frac{Bf_t}{\sqrt{1+(d/\lambda d_0)}}\right)\left(m\frac{\sigma_3}{\min\left(\frac{\sigma_0 d^{(d_f-1)/2}}{\sqrt{1+(d/\lambda d_0)}},\frac{Bf_t}{\sqrt{1+(d/\lambda d_0)}}\right)}+1\right)^{0.5} \quad (5)$$

where σ_0 and f_t represent the characteristic strengths for the ascending and descending zones, respectively; d_f denotes the fractal dimension; d_0 is the maximum aggregate size; and B and λ are dimensionless material constants. The size-dependent failure criterion describes the relationship among the compressive strength, confining pressure and specimen size and is verified against the experimental results for Gosford sandstone.

It is noted that the underlying assumption for the two size-dependent failure criteria above is that the size-effect behaviors in uniaxial and triaxial conditions are similar, supported by experimental results (Hunt 1973; Masoumi et al. 2016b; Medhurst and Brown 1998). Owing to the adoption of the Hoek-Brown failure criterion, the two size-dependent criteria inherit its shortcoming of limited applicability in the brittle regime.

3. Material and methods

3.1 Sample preparation

The slate samples from five blocks collected at the same location in a slate quarry with different diameters of 19, 25, 38, 50, 63 and 75 mm were cored in various directions with respect to foliation planes of 0°, 15°, 30°, 45°, 60° and 90°, as illustrated in Fig. 3a. The slate, exhibiting dark gray to light gray color, possesses a well-developed slaty structure with relatively straight foliation planes. All of the samples, part of which are shown in Fig. 3b, were prepared as per the method suggested by the International Society for Rock Mechanics (ISRM 2007). The length-to-diameter ratio of each specimen was fixed at 2:1. A difficult part of the experimentation lies in obtaining good-quality cores with the required length due to the low success rate, particularly for the foliation-normal cores, which are easy to disk off during coring. Moreover, because of the ambiguity and waviness of foliation planes, the actual foliation orientation may deviate within a range of two to three degrees relative to the specified value of foliation orientation. For this experiment, homogeneous samples were carefully selected, having a relatively uniform composition and no macrodefects visible to the unaided eye. It is worth pointing out that anisotropic materials can be homogenous, which should not be confused with heterogeneity (Simpson 2013). The slate rock used in this experiment has a very fine grain size of 0.01-0.05 mm, and detailed information concerning the petrography and microstructure can be found in the reference (Li et al. 2020a).

3.2 Testing procedure

The laboratory apparatuses for uniaxial and triaxial compression tests are shown in Fig. 4. Uniaxial compression tests were performed on slate samples with diameters of 19, 25, 38, 50, 63 and 75 mm and loading-foliation angles (β) of 0, 15, 30, 45, 60 and 90°. To ensure accuracy, a compression machine with a low loading capacity of 100 kN (see Fig. 4a) was utilized for slate samples with small diameters (19 and 25 mm). For the samples with larger diameters (38, 50, 63 and 75 mm), a stiff testing machine with a 3 MN loading capacity was employed (see Fig.4b). The loading rates for uniaxial compression tests were set identically to be 0.5 MPa/s as the ISRM (2007) suggests. For each specimen, two biaxial strain gauges with a length of 5 mm were used, the arrangements of which are shown in Fig. 2. Throughout the test, the load and strain were simultaneously recorded via a Kyowa datalogger.

In addition, triaxial tests were conducted on slate samples with diameters of 25, 50 and 75 mm and foliation orientations relative to the major principal stress (β) of 0, 15, 30, 45, 60 and 90° using a servo-controlled loading frame system with a capacity of 2 MN and a triaxial cell capable of generating a confining pressure of up to 100 MPa (see Fig. 4c). Three sets of platens incorporating spherical seats 25, 50, and 75 mm in diameter came with the triaxial cell. Moreover, to adapt for the different diameters of the tested samples, three sets of extensometers with different sizes were adopted, each of which included an axial extensometer and a circumferential extensometer with measuring ranges of 10 and 5 mm, respectively. The triaxial compression test was performed according to the individual test suggested by Kovari et al. (1983), in which the individual point on the peak or residual strength envelope is obtained from one test. The loading rates of the confining pressure and axial stress were controlled at 0.05 and 0.5 MPa/s, respectively, as suggested by the ISRM (2007). In this study, slate samples were tested with confining pressures ranging from 1 to 20 MPa.

4. Results and discussion

4.1 Elastic property

As an illustrative example, the typical stress-strain curves of slate samples in uniaxial compression tests are shown Fig. 5. Stress-strain curves No. 1 to 4 correspond to the measured strains at different mounting positions, as displayed in Fig. 2. The results show that axial strains obtained at positions No. 1 and 2 are comparable irrespective of β, while the difference in circumferential strains obtained between the directions of dip and strike (No. 3 and 4) is greatly dependent on β. This demonstrates the existence of elastic anisotropy in slate. The ratios of ε_x/σ_y, ε_y/σ_y and ε_z/σ_y used in section 2.1 to determine the values of E, E', ν, ν' and G' correspond to the secant values at 50% peak stress, as represented by the green lines in Fig. 5.

The five elastic constants determined from slate samples with different sizes under uniaxial compression conditions are listed in Table 1, and each group of results was calculated from the corresponding number of strain gauge readings, collected from samples with different foliation orientations using the least squares method. Taking all five elastic constants into consideration, Kwasniewski (1983) proposed an anisotropy classification for transversely isotropic materials as follows

$$
\begin{aligned}
&w=(2p+q)^{0.5} \\
&p=\left[\left(E/E'-\nu'^{2}\right)/\left(1-\nu^{2}\right)\right]^{0.5} \\
&q=\left[E/G'-2\nu'\left(1+\nu\right)\right]/\left(1-\nu^{2}\right)
\end{aligned}
\tag{6}
$$

According to the anisotropy classification, slate samples 19 mm in diameter and 25 to 75 mm in diameter are classified as low anisotropic rock ($2.1< w\leq 2.5$) and medium anisotropic rock ($2.5< w\leq 3.0$), respectively.

Fig. 6 shows variations in the five elastic constants with the specimen size, as well as comparisons between the results obtained from uniaxial compression and Brazilian tensile tests. The Young's modulus parallel to the isotropic plane generally increases, while the Young's modulus perpendicular to the isotropic plane first decreases and then fluctuates with the specimen size. Both the shear modulus normal to the foliation plane and Poisson's ratios parallel to and perpendicular to the foliation plane vary little throughout the specimen size range. As analyzed in the work of Li et al. (2020a), the combined influence of foliation planes and near-surface damage during sample preparation determines the size effect on the elastic properties in slate. Thus, the outcome of the combined influence for slate in uniaxial compressive conditions is that only the Young's modulus parallel to the isotropic plane presents an increasing size-effect trend, and other elastic constants do not display an evident size-effect trend.

Additionally, with the exception of the Young's modulus parallel to the plane of isotropy, all of the elastic constants obtained by Brazilian tensile tests are higher than those obtained by uniaxial compression tests, regardless of the specimen size. This discrepancy could be attributed to the difference in loading conditions, since rocks have different deformability properties when loaded in tension or compression (Amadei 1996). This also demonstrates that the elastic properties of transversely isotropic rock are stress-dependent, which is consistent with the findings observed in sedimentary rocks (Chiarelli et al. 2003; Corkum and Martin 2007; Masoumi et al. 2016a). Further research is needed on this issue, which is outside of the scope of this study.

4.2 Uniaxial compressive strength

To minimize the influence of heterogeneity, several experiments were performed on slate samples with each prescribed specimen size and foliation orientation. The mean UCS values are summarized in the Supplementary material and plotted in Fig. 8. Based on the experimental results, the size effect and anisotropy in the UCS of slate are investigated in this section.

4.2.1 *Size effect on the UCS*

Similar to the size effect on the tensile strength discussed in Li et al. (2020a) and referring to experimental data shown in Fig. 8, three principles defining the size effect on the UCS of slate should be followed:

(1) The relationship between the UCS and specimen size depends on the mechanical properties of the material.

(2) The variation in the UCS with specimen size shows a descending trend and is closely correlated with the foliation orientation.

(3) For specimens of a prescribed shape, the UCS has upper and lower bounds with varying specimen size.

As stated in the introduction, classical size-effect models are derived from isotropic materials, but they can be important references for exploring the size-effect model applicable to transversely isotropic materials. Based on principle (2), the descending size-effect type, including statistical, size-effect law (SEL) and multifractal scaling law (MFSL) models, is considered. Nevertheless, the MFSL model is not able to describe the strength of an infinitesimal sample, which is infinite as the sample size approaches zero (Masoumi et al. 2015), thereby violating principle (3). At this point, introducing both upper and lower bounds, a transformation of the SEL model expressed by Eq. (7) and a statistical model proposed by Song et al. (2018) expressed by Eq. (8) are compared, thereby fitting the experimental data, as shown in Fig. 7. It is noted that the mean values of the UCS for slate specimens with different diameters at β of 15° are used for the fitting analysis as an illustrative example. Both equations agree well with the experimental data ($R^2 > 0.98$), but the SEL model does not have a reasonable physical meaning for the strength of an infinitesimal sample that is at least one order of magnitude larger than the actual value. Thus, the statistical model is adopted.

$$\sigma_d = \sigma_M + \frac{(\sigma_0 - \sigma_M)}{\sqrt{1 + \dfrac{d}{\lambda d_0}}} \tag{7}$$

$$\sigma_d = \sigma_M + (\sigma_0 - \sigma_M)e^{-kd} \tag{8}$$

where σ_d represents the UCS of the specimen with a diameter of d; σ_0 and σ_M denote the UCS when $d \to 0$ and $d \to \infty$, respectively; λ and d_0 are the same as those in Eq. (5); and k is a parameter related to the mechanical properties of the material.

First, the values of σ_0, σ_M and k at each foliation orientation are obtained from the fitting result based on the mean values of the UCS for specimens with varying sizes. Then, as k is related to the material properties but not dependent on the loading direction, its value is determined by averaging the values of k at different foliation orientations obtained in the previous step. Substituting the constant of k into Eq. (8), the values of σ_0 and σ_M at each foliation orientation are finally determined by repeating the first step. The fitting parameters σ_0, σ_M and k of Eq. (8) are listed in Table 2. The corresponding fitted curves, shown in Fig. 8, are in good agreement with the experimental data with coefficients of determination > 0.92, demonstrating that the UCS of slate follows the descending size-effect trend. The descending size-effect trend is similar to that observed in most isotropic rocks (Darlington et al. 2011; Hoek and Brown 1980), but the severity of the size effect on the UCS of slate changes with the loading-foliation angle. To quantify the influence of anisotropy on the size effect, the derivative of Eq. (8) is utilized in the following form

$$\sigma_d' = -(\sigma_0 - \sigma_M)ke^{-kd} \tag{9}$$

Thus, the severity of the size effect is proportional to the magnitude of $(\sigma_0 - \sigma_M)$ since k is positive for the descending size-effect trend. Overall, the influence of the size effect is reduced as the specimen size increases. Referring to the values of σ_0, σ_M and k listed in Table 2, it is inferred that the strongest and weakest size effects occur at β values of 60° and 30°, respectively.

Furthermore, for a specified loading direction, σ_0 and σ_M predicted by Eq. (8) correspond to the maximum and minimum UCS, respectively, throughout the range of the specimen sizes. The estimated UCS of slate ranges between 66.79 and 237.73 MPa, regardless of the specimen size and loading direction.

4.2.2 *Anisotropy of the UCS*

The experimental UCS data for specimens with diameters of 19, 25, 38, 50, 63 and 75 mm and the predicted data for specimens with sizes approaching both 0 and ∞ versus loading-foliation angle are plotted in Fig. 9, thereby presenting the U-type, which is different from the undulatory-type and shoulder-type as classified by Ramamurthy (1993). For groups with various sample sizes, the maxima of the UCS are located at β of 90°, and the minima of the UCS occur at β of 30° close to (45°-φ), where φ is the friction angle along the foliation plane.

Numerous approaches have been proposed for describing the relationship between the compressive strength and loading direction for transversely isotropic rocks, as reviewed in (Duveau et al. 1998; Li 2019). Among these methods, the empirical equation developed initially by Jaeger (1960) and improved by Donath (1961) is used most commonly in uniaxial compression conditions. The equation is in the following form

$$\sigma_\beta = A - D\cos 2(\beta - \beta_{\min}) \tag{10}$$

where σ_β is the UCS at the loading-foliation angle of β; $\beta_{\min}$ corresponds to the angle at which the UCS is at a minimum; and A and D are two constants. Fitting curves and parameters of both experimental and predicted UCS based on Eq. (10) are plotted in Fig. 9 and summarized in Table 3. The fitting curves agree reasonably well with both the experimental and predicted data. The determined $\beta_{\min}$ fluctuates between 27.7° and 31.3°, with an average angle of 29.2°. The fitting parameter A decreases, while D varies little with the specimen size. It is demonstrated that parameter A is correlated to the size effect. The strength anisotropy is usually represented by the following equation (Ramamurthy 1993):

$$R_c = \frac{\sigma_{c(90)}}{\sigma_{c(\min)}} \tag{11}$$

where R_c is the degree of anisotropy; $\sigma_{c(90)}$ is the UCS at β of 90°; and $\sigma_{c(\min)}$ is the minimum UCS which is commonly in the range for β of 30°-45°. The values of R_c for specimens with diameters of 0 mm, 19 mm, 25 mm, 38 mm, 50 mm, 63 mm, 75 mm and approaching infinity are 1.53, 1.75, 1.76, 1.92, 2.00, 2.13, 1.99 and 2.14, respectively. In general, the degree of strength anisotropy in slate increases with the specimen size, and then stabilizes for samples larger than a critical size.

4.2.3 Universal equation for the UCS

Combining Eqs. (8) and (10), Song et al. (2018) proposed a unified empirical equation describing both the size effect and anisotropy of UCS expressed as

$$\sigma_{c\beta d} = A_M - D_M \cos 2(\beta - \beta_{\min}) + \left[(A_0 - A_M) - (D_0 - D_M)\cos 2(\beta - \beta_{\min})\right] e^{-kd} \tag{12}$$

where $\sigma_{c\beta d}$ is the UCS of a specimen with a diameter of d at a loading-foliation angle of β; A_0 and D_0, A_M and D_M are A and D constants for a specimen size approaching zero or infinite, respectively; and k is a characteristic parameter related to the material, as mentioned in Eq. (8); and $\beta_{\min}$ is the average of β at which the UCS is at a minimum.

The equation fitted by Eq. (12) is as follows:

$$\sigma_{c\beta d} = 120.84 - 48.58\cos 2(\beta - 29.2) + \left[(220.64\text{-}120.84)\text{-}(50.41\text{-}48.58)\cos 2(\beta - 29.2)\right] e^{-0.041d},$$
$$R^2 = 0.933 \tag{13}$$

The experimental data and the fitted surface obtained by Eq. (13) for specimens of different diameters at various loading directions are compared as shown in Fig. 10. The theoretical surface agrees with the experimental data with a high correlation coefficient (R^2 = 0.93). This demonstrates the applicability of the universal equation to slate, a transversely isotropic rock. Accordingly, the universal equation proposed by Song et al. (2018) is recommended for describing the relationship among the UCS, specimen size and loading direction for transversely isotropic rock. It is also a basic step for the further study of the size effect of transversely isotropic rocks in triaxial conditions.

4.3 Triaxial compressive strength

The triaxial compressive strength (TCS), corresponding to the peak axial stresses in stress-strain curves, is extracted from this experiment. The mean TCS values of the slate samples with diameters of 25, 50 and 75 mm at different confining pressures and foliation orientations are summarized in the Supplementary material and shown in Fig. 11.

4.3.1 Size effect on the TCS

As seen in Fig. 11, variations in both the UCS and TCS with regard to the specimen size present a similar trend in line with the observed results in gypsum (Hunt 1973) and sandstone (Masoumi et al. 2016b). Hence, the descending size-effect model applicable to UCS was also utilized to fit the experimental data of the TCS. The fitted curves of the TCS based on Eq. (8) are plotted in Fig. 11, and fitted parameters are obtained as listed in Table 4 with k being a constant of 0.041.

Furthermore, Eq. (9) was employed to quantify the severity of the size effect on the TCS at different foliation angles and confining pressures. As discussed in section 4.2.1, the severity of the size effect is proportional to the magnitude of $(\sigma_0 - \sigma_M)$. Based on the values of $(\sigma_0 - \sigma_M)$ in Table 4, the influence of the confining pressures on the size effect of the compressive strength is weak when β = 0°, 60° and 90°, whereas it is strong when β is in the range of 15° to 45°. When β is located at 15° to 45°, the severity of the size effect on the compressive strength increases with the confining pressure, which is contradictory to the viewpoint (Aubertin et al. 2000) that confining pressures suppress the size effect in rocks. Aubertin et al. (2000) thought that the change from brittle to ductile behavior and the closure of microcracks with increasing confinement diminish the size effect. This discrepancy may be attributed to the unique failure mode, viz., sliding failure along the foliations, observed in the slate at β of 15° to 45° and confining pressures of 0 to 20 MPa. There exists a characteristic confining pressure above which the size dependency starts to diminish as the confining pressure increases, because the failure mode at β of 15° to 45° is transformed to slide across the foliations, resulting in the change from brittle to ductile failure.

For simplification, in this analysis, the size effects on the compressive strength at different confining pressures are assumed to be identical when the samples stay within the brittle regime.

4.3.2 Anisotropy of the TCS

The variations in the triaxial compressive strength of slate samples with diameters of 25, 50 and 75 mm at different confining pressures versus foliation orientations are displayed in Fig. 12, and all the anisotropy curves are U-type curves. The maxima in the anisotropy curves lie at β of 90°, but with increasing confining pressure, the maxima are inclined to shift to β of 0°. The minima of the anisotropy curves are found to shift gradually from β of 30° to β of 45° as the confining pressure increases. Additionally, the anisotropy curves are fitted by Eq. (10) as shown in Fig. 12, and the fitted results are summarized in Table 5. The results indicate that fitted curves based on Eq. (10) agree with the experimental data. The values of parameter A increase as the confining pressures increase, while at the same time, they decrease with increasing specimen size, and the values of parameter D increase with the confining pressure. It has also been observed that the range of the TCS for β of 15°-45° at confining pressures between 0 and 20 MPa decreases as the specimen size increases, particularly for the case at β of 45°. The smaller effect of the confining pressure at β of 15°-45° can be attributed to sliding failure along the foliation planes, which is consistent with the observed results in schist (Duveau et al. 1998).

4.3.3 Size-dependent modified Hoek-Brown failure criterion

To consider the strength anisotropy of intact anisotropic rocks in triaxial conditions, Saroglou and Tsiambaos [34] modified the Hoek-Brown criterion by incorporating an anisotropic parameter k_β in the following form

$$\sigma_1 = \sigma_3 + \sigma_{c\beta}\left(k_\beta m_i \frac{\sigma_3}{\sigma_{c\beta}} + 1\right)^{0.5} \tag{14}$$

where $\sigma_{c\beta}$ represents the UCS of rock at the anisotropic orientation with respect to the loading direction (β); k_β is a parameter describing the anisotropy effect; and m_i is a material constant independent of the loading direction. The parameter $\sigma_{c\beta}$ mainly controls the upward and downward movement of the criterion (Fig. 13a), while k_β influences the curvature of the criterion (Fig. 13b). The modified Hoek-Brown failure criterion has been widely used to predict the failure of various transversely isotropic rocks (Saeidi et al. 2014; Saeidi et al. 2013; Saroglou and Tsiambaos 2008).

As discussed in the previous section, the size dependencies on the UCS and TCS of slate are similar and are thus postulated to be identical for simplification. The size-effect relationship for the UCS (Eq. (12)) is incorporated into the modified Hoek-Brown criterion, thereby resulting in a size-dependent failure criterion that can comprehensively capture the relationship among the compressive strength, anisotropic orientation, specimen size and confining pressure in the following form

$$\sigma_1 = \sigma_3 + \left\{ A_M - D_M \cos 2(\beta - \beta_{\min}) + \left[(A_0 - A_M) - (D_0 - D_M)\cos 2(\beta - \beta_{\min}) \right] e^{-kd} \right\} \times \left(k_\beta m_i \frac{\sigma_3}{\left\{ A_M - D_M \cos 2(\beta - \beta_{\min}) + \left[(A_0 - A_M) - (D_0 - D_M)\cos 2(\beta - \beta_{\min}) \right] e^{-kd} \right\}} + 1\right)^{0.5} \tag{15}$$

First, the values of the parameters in Eq. (12) were calibrated based on UCS data, and the resulting parameters for slate are shown in Eq. (13). The value of m_i was then obtained by fitting the size-dependent modified Hoek-Brown criterion to the compressive strength data obtained at β of 90°, provided that k_β was 1.0, and was further utilized to determine the values of k_β at other anisotropic orientations. The resulting value of m_i is 10.78 for slate. The fitting parameters in Eq. (15) based on uniaxial and triaxial data are summarized in Table 6, and the predicted peak stresses versus the specimen diameter and confining pressure at different loading directions are plotted as cyan surfaces in Fig. 14. The fitted value of k_β decreases initially and then increases with the foliation orientation, reaching a maximum and minimum at β of 0° and β of 45°, respectively. The fitted surfaces agree with the experimental data with coefficients of determination larger than 0.88. Accordingly, the proposed size-dependent modified Hoek-Brown failure criterion is capable of predicting the peak strength of slate under uniaxial and triaxial conditions regardless of the specimen size, foliation orientation or confining pressure. However, inheriting from the basic Hoek–Brown failure criterion, the size-dependent failure criterion is limited to the brittle regime and neglects the influence of intermediate principal stress.

4.3.4 Size-dependent Saeidi failure criterion

To overcome the limitation of the Hoek-Brown failure criterion in the brittle regime, Rafiai (2011) proposed an empirical failure criterion for isotropic rocks that is capable of estimating the strength of rocks in the brittle and ductile failure regimes according to

$$\frac{\sigma_1}{\sigma_{ci}}=\frac{\sigma_3}{\sigma_{ci}}+\left[\frac{1+P(\sigma_3/\sigma_{ci})}{1+Q(\sigma_3/\sigma_{ci})}\right]-\chi \tag{16}$$

where P and Q are two material constants ($P\geq Q\geq 0$) and χ is a reduction factor of strength indicating the fracture degree of the rock mass. Subsequently, Saeidi et al. (2014) extended the failure criterion developed by Rafiai (2011) and proposed a criterion applicable for transversely isotropic rocks, called the Saeidi failure criterion, which is expressed as:

$$\sigma_1=\sigma_3+\sigma_{c\beta}\left[\frac{1+P(\sigma_3/\sigma_{c\beta})}{\alpha_\beta+Q(\sigma_3/\sigma_{c\beta})}\right] \tag{17}$$

where α_β is the reduction factor of the strength associated with the rock anisotropy. In the failure criterion, α_β and $\sigma_{c\beta}$ control the upward and downward movement of the criterion (Fig. 15a and b), and P/Q influences the curvature of the criterion (Fig. 15c). Similar to the size-dependent modified Hoek-Brown failure criterion, the size-dependent Saeidi failure criterion is proposed by including the size effect in the Saeidi failure criterion. As a result, $\sigma_{c\beta}$ in the Saeidi failure criterion is substituted by Eq. (12) according to

$$\sigma_1=\sigma_3+\frac{\left\{A_M-D_M\cos 2(\beta-\beta_{\min})+\left[(A_0-A_M)-(D_0-D_M)\cos 2(\beta-\beta_{\min})\right]e^{-kd}\right\}+P\sigma_3}{\alpha_\beta+Q\sigma_3/\left\{A_M-D_M\cos 2(\beta-\beta_{\min})+\left[(A_0-A_M)-(D_0-D_M)\cos 2(\beta-\beta_{\min})\right]e^{-kd}\right\}} \tag{18}$$

After the size-effect model for UCS is calibrated, the triaxial data are fitted by Eq. (18). The fitted surfaces are plotted as orange surfaces in Fig. 14, and the fitted parameters are listed in Table 6. Compared with the fitted results based on Eq. (15), the data predicted by Eq. (18) agree better with the experimental data with a higher R^2. As seen from the theoretical surfaces in Fig. 14, the size-dependent Saeidi failure criterion fits the experimental data points well, whereas the size-dependent modified Hoek-Brown failure criterion overpredicts the strength at high confining pressures and underpredicts it at intermediate confining pressures at every loading direction. The size-dependent modified Hoek-Brown failure criterion also overpredicts the strength at low confining pressures for β of 30°, 45° and 90°. However, the size-dependent Saeidi failure criterion requires more tests to be performed to determine the parameters in the expression. One common drawback of the two proposed size-dependent failure criteria is that the intermediate principal stress is not considered.

Additionally, to evaluate the applicability of the two size-dependent failure criteria for the estimation of the tensile strength of slate, comparisons between the predicted and measured values are made, as listed in Table 7. σ_t^{p1} and σ_t^{p2} are the values of tensile strength predicted by the size-dependent modified Hoek-Brown and Saeidi failure criteria, respectively. The results indicate that the size-dependent modified Hoek-Brown failure criterion underestimates and overestimates the tensile strength when β is low (0° and 15°) and high (45° - 90°), respectively, and agrees well with the tensile strength at β of 30°. Nevertheless, the size-dependent Saeidi failure criterion continuously underpredicts the tensile strength as β increases from 0° to 45°, while the tensile strength for β of 60°-90° is overpredicted. Moreover, the tensile strength predicted by the two criteria presents a continuously descending size-effect trend, but the tensile strength observed in the laboratory exhibits an initially increasing and then decreasing size-effect trend when the loading-foliation angle is low (0°-30°). Overall, the two proposed failure criteria are incapable of predicting the rock strength in tensile conditions.

4.4 Triaxial residual strength

Since rocks around underground structures (e.g., tunnels, caverns and mining stopes) are still able to sustain certain levels of stress even after they reach the postpeak deformation phase, the residual strength is significant for the safe and optimum design of underground structures (Gao and Kang 2016; Peng and Cai 2019). The residual strength, σ_r, is usually defined as a constant level of stress under which the deformation of existing cracks continues after the peak strength. It can be determined through the flattening trend along the postfailure portion of the stress-strain curve (Tutluoğlu et al. 2015). Due to the extremely brittle nature of the tested slate under uniaxial compression, only the triaxial residual strength (TRS) of the specimens with assorted sizes and foliation orientations was measured at different confining pressures as summarized in the Supplementary material.

4.4.1 Size effect on the TRS

To evaluate whether the residual strength of slate follows a size-effect trend, its variation with the specimen size for three cases of β of 0°, 45° and 90° is shown in Fig. 16. The observed result is that the triaxial residual strength of slate does not present an evident size-effect trend irrespective of the loading direction and confining pressure, which is different from the peak strength. This can be explained as that a brittle or semibrittle material, after being broken, degrades into ductile material with the size effect disappearing (Aubertin et al. 2000).

4.4.2 Anisotropy of the TRS

As seen in Fig. 17, the anisotropy of the triaxial residual strength of slate is very similar for different specimen sizes. When the applied confining pressure is 1 MPa, the residual strength varies little, fluctuating at approximately 25 MPa. As the confining pressure increases from 5 to 20 MPa, the anisotropy of the residual strength increases and presents a U-shaped curve similar to the findings of Liao and Hsieh (1999) in argillite, with the maxima in the anisotropy curves located at β of 0° and the minima shifting from β of 30° to β of 45°.

4.4.3 Modified cohesion loss model

Most recently, Peng and Cai (2019) reviewed various methods, including the Mohr-Coulomb, Joseph-Barron, Hoek-Brown and GSI-softening models, and proposed a cohesion loss model for estimating the residual strength of intact rocks according to

$$\sigma_1 = \sigma_3 + \left(\lambda_i \sigma_c \sigma_3\right)^{0.5} \tag{19}$$

where λ_i is a dimensionless parameter and σ_c represents the UCS of intact rock.

The cohesion loss model is derived from the generalized Hoek-Brown failure criterion by taking the parameter s as zero (the cohesion loss concept) because the value of s is very small (<0.01) when the geological strength index (GSI) is smaller than 60. Moreover, the applicability of the cohesion loss model for various types of intact rocks has been validated. The cohesion loss model has the advantage of passing through the origin in the σ_1-σ_3 space, nonlinearity and a simple form, but neglects the influence of the intermediate principal stress and the inherent anisotropy of rock. To extend the model to estimate the residual strength of transversely isotropic rocks, a modified cohesion loss model is proposed and given as

$$\begin{cases} \sigma_1 = \sigma_3 + \left(\lambda_\beta \sigma_{c\beta} \sigma_3\right)^{0.5} \\ \lambda_\beta = \lambda_m + \left(\lambda_0 - \lambda_m\right) e^{-g\beta} \end{cases} \tag{20}$$

where $\sigma_{c\beta}$ is the UCS at a loading-foliation angle of β, and λ_β is a parameter describing the anisotropy effect as a function of β, and λ_0, λ_m and g are constants.

The experimental residual strength of slate with different specimen sizes at different loading directions as well as fitted curves based on the modified cohesion loss model are depicted in Fig. 18, and their fitting parameters are summarized in Table 8. The results indicate that the modified cohesion loss model effectively captures the relationship between the residual strength and confining pressure for slate in this study. To the author's knowledge, little research in relation to the residual strength of transversely isotropic rocks takes the anisotropy effect into consideration. Although the residual strength data of argillite were obtained at different confining pressures and anisotropic orientations (Liao and Hsieh 1999), the corresponding UCS data were unknown due to the adopted multiple-failure-state test method. Thus, the published data cannot be used to validate the model. In the future, more systematic investigations into the residual behavior are needed to explore the applicability of the modified cohesion loss model to other transversely isotropic rocks.

Additionally, the parameter λ_β varies little with the specimen size, whereas its variation with β is evident as illustrated in Fig. 19. The parameter λ_β gradually decreases as β increases, i.e., $\lambda_\beta = 2.73 + 2.83e^{-0.055\beta}$, attaining the maxima and minima at β of 0° and 90°, respectively. Overall, λ_β for the slate ranges between 2 and 6. The major difference in λ_β again demonstrates that an anisotropy effect on the residual strength of slate exists.

4.4.4 *Brittleness index*

Based on the reported peak and residual strengths in the previous sections, the brittleness characteristics of slate under triaxial conditions are evaluated. The definition of the brittleness index (BI) = 1-*TRS/TCS* is adopted in this study, which has been recommended to quantify the brittleness of the rock and rock mass (Roshan et al. 2017; Yang et al. 2020). BI ranges from 1 to 0, reflecting the transition from brittleness to ductility. The BI variations of different transversely isotropic rocks, including sandstone (Gowd and Rummel 1980; Roshan et al. 2017; Yang et al. 2012), schist and gneiss (Kumar et al. 2010), mudstone (Lu et al. 2010), limestone and marble (Walton et al. 2015) and slate (this study), with the confining pressure, are compiled and compared as shown in Fig. 21. The results show that BI decreases as a function of confining pressure for transversely isotropic rocks, following the cohesion-weakening-friction-strengthening (CWFS) model for the brittle failure of rock, as demonstrated and verified by Hajiabdolmajid et al. (2002) and Martin and Chandler (1994). The model has also been supported recently by both numerical (Gao and Kang 2016) and experimental results (Rafiei Renani and Martin 2018; Walton et al. 2018). As illustrated in Fig. 20, when a rock material is undergoing a triaxial compression test, the cohesive strength is mobilized from an initial state and then decreases from the onset of microcracking to the residual stage with increasing crack density, while the frictional strength is mobilized at the onset of microcracking and then accumulates until it is fully completed when macrocracks are formed. After increasing the confining pressure, the mobilization of the cohesive strength displays limited alteration, but that of the normal stress-dependent frictional strength increases significantly, especially at the residual phase when the frictional strength is fully mobilized. Consequently, both the peak and residual strengths increase at higher confinement; nevertheless, the residual strength increases at a higher rate. This can also account for the importance of support applications in solving the issue of the unstable collapse of underground structures.

Additionally, based on the compiled data shown in Fig. 21, the lower and upper bounds of the relationship between BI and σ_3 for transversely isotropic rocks are proposed by the following two functions.

(1) Lower bound:

$$BI = 0.56 - 0.077\sigma_3^{0.6} \tag{21}$$

(2) Upper bound:

$$BI = 1 - 0.061\sigma_3^{0.6} \tag{22}$$

It should be noted that the proposed equations are only applicable to rocks in the brittle failure regime. Interestingly, the confining pressure corresponding to the plastic end of the lower bound is approximately 105 MPa, coinciding with the UCS on the brittle end for various rock types (Tutluoğlu et al. 2015). It agrees with the statistical analysis of the data from more than 1,100 triaxial tests in Singh et al. (2011) that the critical confining pressure for an intact rock can be taken as its UCS.

BI does not present an evident size effect, and neither does the residual strength. The average BI obtained from slate specimens of different sizes was calculated, the variation of which with β is depicted in Fig. 22. At different confining pressures, the BI values generally decrease first and then increase as β increases, exhibiting a U-type shape, with the minima and maxima located at β of 30° and 90°, respectively. This implies that the failure of slate specimens at β values of 30° and 90° displays the lowest and highest brittleness, respectively, throughout the range of confining pressures.

5. Conclusions

In this study, the size effect and anisotropy of slate, as a transversely isotropic rock, were investigated based on compression tests performed on slate samples of different sizes at different confining pressures and foliation orientations with respect to the direction of the major principal stress. The main conclusions are summarized as follows:

(1) The Young's modulus parallel to the transversely isotropic plane exhibits an ascending size-effect trend, while the other four elastic constants are insensitive to the specimen size.

(2) A descending size-effect relation developed from coal is extended to slate, which captures the relationship among the uniaxial compressive strength, specimen size and loading direction.

(3) The anisotropy of the compressive strength is evident, presenting a U-type, which increases with the specimen size and stabilizes for samples larger than a critical size. Additionally, the anisotropy of the compressive strength is captured by a cosine relation.

(4) The size-effect behaviors of the uniaxial and triaxial compressive strengths are similar. By incorporating the size-effect relation for the uniaxial compressive strength into the modified Hoek-Brown and Saeidi failure criteria, two size-dependent failure criteria are

proposed and verified against the experimental slate data. They are capable of describing the relationship among the specimen size, confining pressure, foliation orientation and rock strength under uniaxial and triaxial compressive conditions in the brittle regime. The size-dependent Saeidi failure criterion is superior to the size-dependent modified Hoek-Brown failure criterion in terms of prediction accuracy with a higher nonlinearity.

(5) An evident anisotropy effect is observed in the triaxial residual strength of slate. A cohesion loss model is modified to capture the anisotropic residual strength, in which the influence of anisotropy decreases with increasing foliation orientation. Two equations delineating the upper and lower bounds for the brittleness index are proposed for transversely isotropic rocks.

Acknowledgements

The research work presented in this paper is financially supported by the National Natural Science Foundation of China (Grant Nos. 51774322 and 41807241). The authors would like to thank the editor and anonymous reviewers for their constructive comments, which have greatly improved this paper.

References

Amadei B (1996) Importance of anisotropy when estimating and measuring in situ stresses in rock. International Journal of Rock Mechanics and Mining Sciences & Geomechanics Abstracts 33:293-325 doi:https://doi.org/10.1016/0148-9062(95)00062-3

Amadei B (2012) Rock anisotropy and the theory of stress measurements. vol 2. Springer Science & Business Media,

Aubertin M, Li L, Simon R (2000) A multiaxial stress criterion for short- and long-term strength of isotropic rock media International Journal of Rock Mechanics and Mining Sciences 37:1169-1193 doi:https://doi.org/10.1016/S1365-1609(00)00047-2

Bažant ZP (1984) Size effect in blunt fracture: concrete, rock, metal Journal of Engineering Mechanics 110:518-535

Bažant ZP (1997) Scaling of quasibrittle fracture: hypotheses of invasive and lacunar fractality, their critique and Weibull connection International Journal of Fracture 83:41-65 doi:10.1023/a:1007335506684

Benz T, Schwab R, Kauther RA, Vermeer PA (2008) A Hoek–Brown criterion with intrinsic material strength factorization. International Journal of Rock Mechanics and Mining Sciences 45:210-222 doi:https://doi.org/10.1016/j.ijrmms.2007.05.003

Broch E, Franklin JA (1972) The point-load strength test International Journal of Rock Mechanics and Mining Sciences & Geomechanics Abstracts 9:669-676 doi:https://doi.org/10.1016/0148-9062(72)90030-7

Carpinteri A, Chiaia B, Ferro G (1995) Size effects on nominal tensile strength of concrete structures: multifractality of material ligaments and dimensional transition from order to disorder Materials and Structures 28:311 doi:10.1007/bf02473145

Chen Y, Lin H, Ding X, Xie S (2021) Scale effect of shear mechanical properties of non-penetrating horizontal rock-like joints Environmental Earth Sciences 80:192 doi:10.1007/s12665-021-09485-x

Chiarelli AS, Shao JF, Hoteit N (2003) Modeling of elastoplastic damage behavior of a claystone International Journal of Plasticity 19:23-45 doi:https://doi.org/10.1016/S0749-6419(01)00017-1

Cho J-W, Kim H, Jeon S, Min K-B (2012) Deformation and strength anisotropy of Asan gneiss, Boryeong shale, and Yeoncheon schist International Journal of Rock Mechanics and Mining Sciences 50:158-169 doi:https://doi.org/10.1016/j.ijrmms.2011.12.004

Corkum AG, Martin CD (2007) The mechanical behaviour of weak mudstone (Opalinus Clay) at low stresses International Journal of Rock Mechanics and Mining Sciences 44:196-209 doi:https://doi.org/10.1016/j.ijrmms.2006.06.004

Darbor M, Faramarzi L, Sharifzadeh M (2019) Size-dependent compressive strength properties of hard rocks and rock-like cementitious brittle materials Geosystem Engineering 22:179-192

Darlington WJ, Ranjith PG, Choi SK (2011) The Effect of Specimen Size on Strength and Other Properties in Laboratory Testing of Rock and Rock-Like Cementitious Brittle Materials. Rock Mechanics and Rock Engineering 44:513-529 doi:10.1007/s00603-011-0161-6

Donath FA (1961) Experimental study of shear failure in anisotropic rocks. Geological Society of America Bulletin 72:985-989

Duveau G, Shao J, Henry J (1998) Assessment of some failure criteria for strongly anisotropic geomaterials. Mechanics of Cohesive‐frictional Materials 3:1-26

Elkadi AS, Van Mier JGM, Sluys LJ (2006) Multiaxial failure of low-cohesive frictional materials: fracture behaviour and size dependency. Philosophical Magazine 86:3137-3159 doi:10.1080/14786430500156351

Gao FQ, Kang HP (2016) Effects of pre-existing discontinuities on the residual strength of rock mass – Insight from a discrete element method simulation Journal of Structural Geology 85:40-50 doi:https://doi.org/10.1016/j.jsg.2016.02.010

Gowd T, Rummel F Effect of confining pressure on the fracture behaviour of a porous rock. In: International Journal of Rock Mechanics and Mining Sciences & Geomechanics Abstracts, 1980. vol 4. Elsevier, pp 225-229

Hajiabdolmajid V, Kaiser PK, Martin CD (2002) Modelling brittle failure of rock. International Journal of Rock Mechanics and Mining Sciences 39:731-741 doi:https://doi.org/10.1016/S1365-1609(02)00051-5

Han D, Li K, Meng J (2020a) Evolution of nonlinear elasticity and crack damage of rock joint under cyclic tension International Journal of Rock Mechanics and Mining Sciences 128:104286

Han DY, Zhu JB, Leung YF (2020b) Deformation of healed rock joints under tension: experimental study and empirical model 53(7): 3353–3362

Hawkins AB (1998) Aspects of rock strength Bulletin of Engineering Geology and the Environment 57:17-30 doi:10.1007/s100640050017

Hoek E, Brown ET (1980) Underground excavations in rock. Institution of Mining and Metallurgy, Spon Press, Hertford, London

Hunt DD (1973) The influence of confining pressure on size effect., Massachusetts Institute of Technology

ISRM (2007) The complete suggested methods for rock characterization, testing and monitoring: 1974–2006. Compilation Arranged by the ISRM Turkish National Group, Ankara, Turkey

Jaeger J (1960) Shear failure of anistropic rocks Geological Magazine 97:65-72

Kovari K, Tisa A, Einstein H, Franklin J (1983) Suggested methods for determining the strength of rock materials in triaxial compression: revised version. Journal of Rock Mechanics and Mining Sciences & Geomechanics Abstracts

Kumar R, Sharma KG, Varadarajan A (2010) Post-peak response of some metamorphic rocks of India under high confining pressures. International Journal of Rock Mechanics and Mining Sciences 47:1357-1362 doi:https://doi.org/10.1016/j.ijrmms.2010.08.016

Kwasniewski M (1983) Anisotropy of elasticity of rocks and its effect on the magnitude and distribution of stresses around underground openings Proceedings of the 8th Plenary Scientific Session of the International Bureau of Strata Mechanics: Application of Rock Mechanics to Planning and Design Prior to Mining:5-37

Li K (2019) Size effect and anisotropy in transversely isotropic rocks. The Hong Kong Polytechnic University

Li K, Cheng Y, Fan X (2018) Roles of model size and particle size distribution on macro-mechanical properties of Lac du Bonnet granite using flat-joint model Computers and Geotechnics 103:43-60 doi:https://doi.org/10.1016/j.compgeo.2018.07.007

Li K, Cheng Y, Yin Z-Y, Han D, Meng J (2020a) Size Effects in a Transversely Isotropic Rock Under Brazilian Tests: Laboratory Testing Rock Mechanics and Rock Engineering 53:2623-2642 doi:10.1007/s00603-020-02058-7

Li K, Yin Z-Y, Cheng Y, Cao P, Meng J (2020b) Three-dimensional discrete element simulation of indirect tensile behaviour of a transversely isotropic rock International Journal for Numerical and Analytical Methods in Geomechanics 44:1812-1832 doi:10.1002/nag.3110

Liao J, Hsieh H Triaxial residual strength of an anisotropic rock. In: Vail Rocks 1999, The 37th US Symposium on Rock Mechanics (USRMS), 1999. American Rock Mechanics Association,

Lu Y, Wang L, Yang F, Li Y, Chen H (2010) Post-peak strain softening mechanical properties of weak rock. Chinese Journal of Rock Mechanics and Engineering 29:640-648

Ma T, Peng N, Zhu Z, Zhang Q, Yang C, Zhao J (2018) Brazilian Tensile Strength of Anisotropic Rocks: Review and New Insights. Energies 11:304

Martin C, Chandler N (1994) The progressive fracture of Lac du Bonnet granite International Journal of Rock Mechanics and Mining Sciences & Geomechanics Abstracts 31:643-659

Masoumi H (2013) Investigation into the mechanical behaviour of intact rock at different sizes. University of New South Wales

Masoumi H, Douglas KJ, Russell AR (2016a) A Bounding Surface Plasticity Model for Intact Rock Exhibiting Size-Dependent Behaviour Rock Mechanics and Rock Engineering 49:47-62 doi:10.1007/s00603-015-0744-8

Masoumi H, Roshan H, Hagan PC (2016b) Size-Dependent Hoek-Brown Failure Criterion International Journal of Geomechanics 17:04016048

Masoumi H, Roshan H, Hedayat A, Hagan PC (2018) Scale-Size Dependency of Intact Rock under Point-Load and Indirect Tensile Brazilian Testing International Journal of Geomechanics 18:04018006

Masoumi H, Saydam S, Hagan PC (2015) Unified size-effect law for intact rock International Journal of Geomechanics 16:04015059

Masoumi H, Serati M, Williams DJ, Alehossein H Size dependency of intact rocks with high brittleness: A potential solution to eliminate secondary fractures in Brazilian test. In: 51st US Rock Mechanics/Geomechanics Symposium, 2017. American Rock Mechanics Association,

Medhurst TP, Brown ET (1998) A study of the mechanical behaviour of coal for pillar design International Journal of Rock Mechanics and Mining Sciences 35:1087-1105 doi:https://doi.org/10.1016/S0148-9062(98)00168-5

Meier T, Rybacki E, Backers T, Dresen G (2015) Influence of Bedding Angle on Borehole

Stability: A Laboratory Investigation of Transverse Isotropic Oil Shale Rock Mechanics and Rock Engineering 48:1535-1546 doi:10.1007/s00603-014-0654-1

Nishimatsu Y, Yamagushi U, Motosugi K, Morita M (1969) The size effect and experimental error of the strength of rocks. Journal of the Society of Materials Science, Japan 18:1019-1025

Pei J (2008) Strength of transversely isotropic rocks. Massachusetts Institute of Technology

Peng J, Cai M (2019) A cohesion loss model for determining residual strength of intact rocks International Journal of Rock Mechanics and Mining Sciences 119:131-139 doi:https://doi.org/10.1016/j.ijrmms.2019.03.032

Pierce M, Gaida M, DeGagne D Estimation of rock block strength. In: Proceedings of the 3rd Canada–US rock mechanical symposium, Toronto, 2009.

Quiñones J, Arzúa J, Alejano LR, García-Bastante F, Mas Ivars D, Walton G (2017) Analysis of size effects on the geomechanical parameters of intact granite samples under unconfined conditions Acta Geotechnica 12:1229–1242 doi:10.1007/s11440-017-0531-7

Rafiai H (2011) New empirical polyaxial criterion for rock strength International Journal of Rock Mechanics and Mining Sciences 48:922-931 doi:https://doi.org/10.1016/j.ijrmms.2011.06.014

Rafiei Renani H, Martin CD (2018) Cohesion degradation and friction mobilization in brittle failure of rocks. International Journal of Rock Mechanics and Mining Sciences 106:1-13 doi:https://doi.org/10.1016/j.ijrmms.2018.04.003

Ramamurthy T (1993) Strength and modulus responses of anisotropic rocks. Comprehensive rock engineering 1:313-329

Rocco C, Guinea GV, Planas J, Elices M (1999a) Size effect and boundary conditions in the Brazilian test: Experimental verification. Materials and Structures 32:210 doi:10.1007/bf02481517

Rocco C, Guinea GV, Planas J, Elices M (1999b) Size effect and boundary conditions in the brazilian test: theoretical analysis. Materials and Structures 32:437 doi:10.1007/BF02482715

Roshan H, Masoumi H, Regenauer-Lieb K (2017) Frictional behaviour of sandstone: A sample-size dependent triaxial investigation Journal of Structural Geology 94:154-165 doi:https://doi.org/10.1016/j.jsg.2016.11.014

Saeidi O, Rasouli V, Vaneghi RG, Gholami R, Torabi SR (2014) A modified failure criterion for transversely isotropic rocks Geoscience Frontiers 5:215-225 doi:https://doi.org/10.1016/j.gsf.2013.05.005

Saeidi O, Vaneghi RG, Rasouli V, Gholami R (2013) A modified empirical criterion for strength of transversely anisotropic rocks with metamorphic origin. Bulletin of Engineering

Geology and the Environment 72:257-269 doi:10.1007/s10064-013-0472-9

Saroglou H, Tsiambaos G (2008) A modified Hoek–Brown failure criterion for anisotropic intact rock International Journal of Rock Mechanics and Mining Sciences 45:223-234 doi:https://doi.org/10.1016/j.ijrmms.2007.05.004

Simpson NDJ (2013) An analysis of tensile strength, fracture initiation and propagation in anisotropic rock (gas shale) using Brazilian tests equipped with high speed video and acoustic emission. Institutt for petroleumsteknologi og anvendt geofysikk

Singh M, Raj A, Singh B (2011) Modified Mohr–Coulomb criterion for non-linear triaxial and polyaxial strength of intact rocks International Journal of Rock Mechanics and Mining Sciences 48:546-555 doi:https://doi.org/10.1016/j.ijrmms.2011.02.004

Song H, Jiang Y, Elsworth D, Zhao Y, Wang J, Liu B (2018) Scale effects and strength anisotropy in coal. International Journal of Coal Geology 195:37-46 doi:https://doi.org/10.1016/j.coal.2018.05.006

Thuro K, Plinninger R Scale effects in rock strength properties Part 2: Point load test and point load strength index. In: Proceedings of the ISRM Regional Symposium Eurock, 2001. pp 175-180

Thuro K, Plinninger R, Zäh S, Schütz S (2001) Scale effects in rock strength properties. Part 1: Unconfined compressive test and Brazilian test. EUROCK 2001: Rock Mechanics□ A Challenge for Society:169-174

Tutluoğlu L, Öge İF, Karpuz C (2015) Relationship Between Pre-failure and Post-failure Mechanical Properties of Rock Material of Different Origin. Rock Mechanics and Rock Engineering 48:121-141 doi:10.1007/s00603-014-0549-1

Walton G, Alejano LR, Arzua J, Markley T (2018) Crack Damage Parameters and Dilatancy of Artificially Jointed Granite Samples Under Triaxial Compression. Rock Mechanics and Rock Engineering doi:10.1007/s00603-018-1433-1

Walton G, Arzúa J, Alejano LR, Diederichs MS (2015) A Laboratory-Testing-Based Study on the Strength, Deformability, and Dilatancy of Carbonate Rocks at Low Confinement. Rock Mechanics and Rock Engineering 48:941-958 doi:10.1007/s00603-014-0631-8

Weibull W (1951) A statistical distribution function of wide applicability. Journal of applied mechanics 18:293-297

Wilson AH (1983) The stability of underground workings in the soft rocks of the Coal Measures International Journal of Mining Engineering 1:91-187 doi:10.1007/bf00880785

Wittke W (2014) Rock mechanics based on an anisotropic jointed rock model (AJRM). John Wiley & Sons,

Yang S-Q, Jing H-W, Wang S-Y (2012) Experimental Investigation on the Strength, Deformability, Failure Behavior and Acoustic Emission Locations of Red Sandstone Under Triaxial Compression. Rock Mechanics and Rock Engineering 45:583-606 doi:10.1007/s00603-011-0208-8

Yang S-Q, Yin P-F, Ranjith PG (2020) Experimental Study on Mechanical Behavior and Brittleness Characteristics of Longmaxi Formation Shale in Changning, Sichuan Basin, China Rock Mechanics and Rock Engineering doi:10.1007/s00603-020-02057-8

Yoshinaka R, Osada M, Park H, Sasaki T, Sasaki K (2008) Practical determination of mechanical design parameters of intact rock considering scale effect. Engineering Geology 96:173-186 doi:https://doi.org/10.1016/j.enggeo.2007.10.008

Zhai H, Masoumi H, Zoorabadi M, Canbulat I (2020) Size-dependent Behaviour of Weak Intact Rocks Rock Mechanics and Rock Engineering doi:10.1007/s00603-020-02117-z

Zhang Q, Zhu H, Zhang L, Ding X (2011) Study of scale effect on intact rock strength using particle flow modeling. International Journal of Rock Mechanics and Mining Sciences 48:1320-1328 doi:http://dx.doi.org/10.1016/j.ijrmms.2011.09.016

Zheng Y, Chen C, Liu T, Song D, Meng F (2019) Stability analysis of anti-dip bedding rock slopes locally reinforced by rock bolts Engineering Geology 251:228-240 doi:https://doi.org/10.1016/j.enggeo.2019.02.002

Tables

Table 1 The five elastic constants determined on the slate samples with different diameters using uniaxial compression tests

Diameter (mm)	Number of gauges	E (GPa)	E' (GPa)	ν	ν'	G' (GPa)	w
19	48	58.86	49.29	0.16	0.20	19.01	2.2
25	68	71.58	34.39	0.20	0.16	15.41	2.7
38	48	72.26	25.08	0.21	0.17	17.32	2.7
50	56	71.53	36.40	0.19	0.15	11.82	3.0
63	44	81.43	37.60	0.19	0.18	13.62	3.0
75	52	86.73	33.47	0.17	0.19	18.01	2.8

Table 2 Fitting parameters in Eq. (8) for UCS of slate specimens with different sizes loaded at different loading-foliation angles

β (°)	0	15	30	45	60	90
σ_0 (MPa)	197.32	180.30	155.16	169.28	222.37	237.73
σ_M (MPa)	97.18	81.95	66.79	73.75	106.70	142.88
$\sigma_0 - \sigma_M$ (MPa)	100.14	98.35	88.37	95.53	115.67	94.85
k	0.041					
R^2	0.93	0.99	0.97	0.94	1.00	0.93

Table 3 Parameters in Eq. (10) for the slate specimens of different diameters under uniaxial compression

Diameter (mm)	$d \to 0$	19	25	38	50	63	75	$d \to \infty$
β_{min} (°)	27.7	28.9	28.1	29.2	31.3	29.7	27.7	29.6
A	219.37	168.41	150.83	145.46	137.46	127.15	123.35	121.18
D	48.91	50.97	44.18	50.82	53.00	50.14	44.96	49.01
R^2	0.79	0.91	0.86	0.94	0.93	0.92	0.97	0.96

Table 4 Comparison of values of $(\sigma_0 - \sigma_M)$ at different confining pressures and foliation orientations

β (°)	0					15				
σ_3	0	1	5	10	20	0	1	5	10	20
σ_0	197.3	180.6	206.8	326.9	322.3	180.3	192.1	299.1	359.5	381.0
σ_M	97.2	121.7	162.0	173.0	244.9	81.9	86.1	100.7	113.3	148.6
$\sigma_0 - \sigma_M$	100.1	58.9	44.8	153.9	77.4	98.4	106.0	198.4	246.2	232.4
β (°)	30					45				
σ_3	0	1	5	10	20	0	1	5	10	20
σ_0	155.2	189.5	229.9	312.3	374.8	169.3	200.9	254.2	305.9	383.6
σ_M	66.8	68.8	85.6	91.6	128.6	73.8	77.8	92.9	95.4	116.4
$\sigma_0 - \sigma_M$	88.4	120.7	144.3	220.7	246.2	95.5	123.1	161.3	210.5	267.2
β (°)	60					90				
σ_3	0	1	5	10	20	0	1	5	10	20
σ_0	222.4	253.4	240.2	276.5	381.9	237.7	194.3	316.5	307.1	351.4
σ_M	106.7	108.0	134.0	160.7	181.9	142.9	166.8	173.5	207.4	247.3
$\sigma_0 - \sigma_M$	115.7	145.4	106.2	115.8	200.0	94.8	27.5	143.0	99.7	104.1

Table 5 Parameters in Eq. (10) for the slate specimens of 25, 50 and 75 mm in diameter loaded at different confining pressures

Confining pressures (MPa)		0	1	5	10	20
$d = 25$ mm	β_{min} (°)	28.1	27.6	34.7	40.7	38.5
	A	150.83	160.05	201.27	235.02	279.24
	D	44.18	40.01	55.66	60.55	61.38
	R^2	0.86	0.85	0.93	0.93	0.89
$d = 50$ mm	β_{min} (°)	31.33	31.06	34.59	34.33	39.02
	A	137.46	150.47	190.01	214.03	251.50
	D	53.00	56.73	72.31	83.36	86.31
	R^2	0.93	0.94	0.90	0.86	0.81
$d = 75$ mm	β_{min} (°)	27.7	34.1	38.6	36.9	40.7
	A	123.35	145.49	162.18	189.87	250.15
	D	44.96	68.24	66.67	81.38	116.30
	R^2	0.97	0.97	0.89	0.90	0.91

Table 6 Parameters in Eqs. (15) and (18) for the slate specimen loaded at different confining pressures

β (°)		0	15	30	45	60	90
Size-dependent modified H-B failure criterion	k_β	1.91	1.09	0.76	0.57	1.14	1.00
	R^2	0.98	0.89	0.93	0.88	0.92	0.95
Size-dependent Saeidi failure criterion	α_β	0.96	0.98	1.08	1.07	0.91	1.03
	A	13.73	20.99	11.82	22.82	9.11	16.73
	B	3.74	9.98	4.96	13.93	3.44	8.23
	R^2	0.98	0.94	0.93	0.91	0.95	0.96

Table 7 Comparisons between the measured tensile strength by experiment (Li et al. 2020a) and the predicted one by size-dependent failure criteria

Diameter (mm)	β =0°			β =15°			β =30°		
	σ_t^m (MPa)	σ_t^{p1} (MPa)	σ_t^{p2} (MPa)	σ_t^m (MPa)	σ_t^{p1} (MPa)	σ_t^{p2} (MPa)	σ_t^m (MPa)	σ_t^{p1} (MPa)	σ_t^{p2} (MPa)
25	19.60	6.34	9.07	17.50	9.55	5.27	10.19	12.94	8.59
38	21.95	5.63	8.05	19.23	8.32	4.59	13.36	11.19	7.43
50	20.15	5.24	7.49	13.33	7.65	4.22	12.50	10.22	6.79
63	16.47	4.99	7.13	14.20	7.21	3.98	9.30	9.60	6.37
75	12.45	4.85	6.92	11.53	6.96	3.84	9.30	9.25	6.14
100	12.55	4.70	6.72	10.41	6.72	3.71	9.01	8.90	5.91
Diameter (mm)	β =45°			β =60°			β =90°		
	σ_t^m (MPa)	σ_t^{p1} (MPa)	σ_t^{p2} (MPa)	σ_t^m (MPa)	σ_t^{p1} (MPa)	σ_t^{p2} (MPa)	σ_t^m (MPa)	σ_t^{p1} (MPa)	σ_t^{p2} (MPa)
25	13.10	18.17	4.93	9.20	10.74	13.78	9.10	16.78	10.56
38	12.20	15.86	4.30	8.98	9.56	12.27	8.66	15.41	9.69
50	10.16	14.59	3.96	7.57	8.91	11.43	4.87	14.65	6.21
63	8.69	13.76	3.73	5.34	8.48	10.88	6.61	14.16	8.90
75	10.05	13.30	3.61	6.71	8.25	10.58	5.66	13.88	8.73
100	5.95	12.84	3.48	4.84	8.01	10.28	3.32	13.61	8.56

Table 8 Fitting parameters of Eq. (20) for residual strengths of slate samples loaded at different loading directions

β (°)		0	15	30	45	60	90
	$\sigma_{c\beta}$	129.5	115.6	96.1	107.0	147.7	169.1
d = 25 mm	λ_β	5.1	4.0	3.6	3.4	3.0	2.4
	R^2	0.99	0.94	0.85	0.94	1.00	0.94
	$\sigma_{c\beta}$	115.2	95.9	78.8	82.5	121.9	157.2
d = 50 mm	λ_β	6.0	3.4	4.8	2.6	3.7	2.4
	R^2	0.99	0.98	0.69	0.97	0.93	0.95
	$\sigma_{c\beta}$	97.3	87.6	73.7	82.2	110.8	146.7
d = 75 mm	λ_β	5.9	3.3	2.7	2.3	3.4	2.1
	R^2	1.00	0.98	0.98	0.98	0.77	0.97

Figure captions

Fig. 1 The cylindrical geometry of a transversely isotropic material under compression

Fig. 2 The schematic diagram and real image of biaxial strain gauges glued on the specimens in uniaxial compression tests with: $\beta = 0°$ (a) and (d); $0° < \beta < 90°$ (b) and (e); $\beta = 90°$ (c) and (f)

Fig. 3 Preparation of specimens with different diameters and foliation orientations: (a) coring of specimens with different orientations; (b) part of specimens in each size used in the compression test

Fig. 4 The testing equipment for: (a) uniaxial compression tests on 19- and 25-mm-diameter samples and (b) on 38-, 50-, 63- and 75-mm-diameter samples, (c) triaxial compression tests on 25-, 50- and 75-mm-diameter samples

Fig. 5 Typical stress-strain curves of slate specimens under uniaxial compression tests: (a) β =0°; (b) β =45° and (c) β =90°

Fig. 6 Variations of five elastic constants with specimen size, and comparisons between results obtained from uniaxial compression and Brazilian tensile tests (Li et al. 2020a): (a) E, E', G' and (b) v, v'. The solid and dashed lines represent the results obtained from uniaxial compression and Brazilian tensile tests, respectively

Fig. 7 Comparison between fitting results of Eqs. (7) and (8)

Fig. 8 Size effects on UCS of slate specimens loaded at different loading-foliation angles

Fig. 9 Anisotropy in UCS of slate samples with different sizes

Fig. 10 Comparison between experimental data and a theoretical surface obtained by Eq. (13) for specimens of different diameters at various loading directions

Fig. 11 Compressive strength versus sample diameter and fitted curves based on Eq. (8) at different confining pressures and loading directions: (a) β =0°; (b) β =15°; (c) β =30°; (d) β =45°; (e) β =60° and (f) β =90°

Fig. 12 Variations of UCS and TCS of slate with different specimen diameters versus β: (a) d=25mm, (b) d=50mm and (c) d=75mm

Fig. 13 Schematic representation of the modified Hoek-Brown failure criterion: (a) at different

$\sigma_{c\beta}$ values and identical k_β of 1.0 and m_i of 10; and (b) at different k_β values and identical $\sigma_{c\beta}$ of 100MPa and m_i of 10

Fig. 14 Comparisons between applicability of proposed size-dependent failure criteria based on the modified Hoek-Brown criterion and the Saeidi criterion to the compressive strength obtained from slate samples with different sizes at different confining pressures and loading directions: (a) β =0°; (b) β =15°; (c) β =30°; (d) β =45°; (e) β =60° and (f) β =90°. The cyan surface represents the size-dependent modified Hoek-Brown failure criterion. The orange surface represents the size-dependent Saeidi failure criterion

Fig. 15 Schematic representation of the Saeidi failure criterion: (a) at different α values and identical $\sigma_{c\beta}$ of 100MPa, A of 10 and B of 2; (b) at different $\sigma_{c\beta}$ values and identical α of 0.5, A of 10 and B of 2; and (c) at different ratios of A/B and identical $\sigma_{c\beta}$ of 100MPa, α of 0.5 and A of 10

Fig. 16 Triaxial residual strength versus sample diameter at different confining pressures and loading directions: (a) β =0°; (b) β =45°; and (c) β =90°

Fig. 17 Variation of triaxial residual strength of slate with different specimen diameters versus β: (a) d=25mm and (b) d=75mm

Fig. 18 Experimental values of triaxial residual strength and fitted curves based on the modified cohesion loss model for slate samples with different sizes: (a) d=25mm; (b) d=50mm and (c) d=75mm

Fig. 19 Variation of parameters λ_β with β

Fig. 20 Mobilization of the cohesive and frictional strength in the CWFS model, from Gao and Kang (2016). c_i and c_r represent the initial and residual cohesive strength, respectively; ΔF_p and ΔF_r denote the increasement in frictional strength due to the increased confinement at the peak and residual stage, respectively; $\Delta\sigma_p$ and $\Delta\sigma_r$ refer to the increased peak and residual strength due to increased confining pressure, respectively

Fig. 21 Variations of BI as a function of confining pressures for transversely isotropic rocks

Fig. 22 Variation of average BI with β for slate

Fig. 1

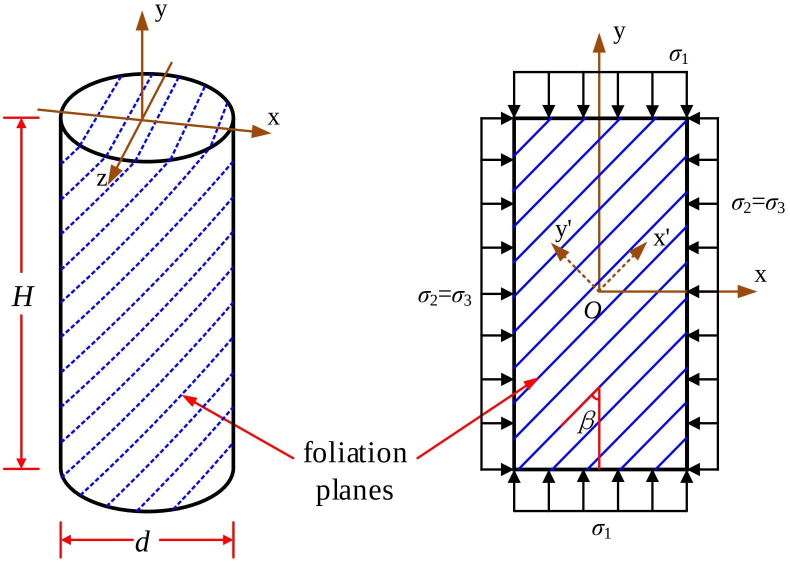

y
x
z
H
d
foliation planes
y
x
σ_1
$\sigma_2=\sigma_3$
$\sigma_2=\sigma_3$
y'
x'
O
β
σ_1

Fig. 2

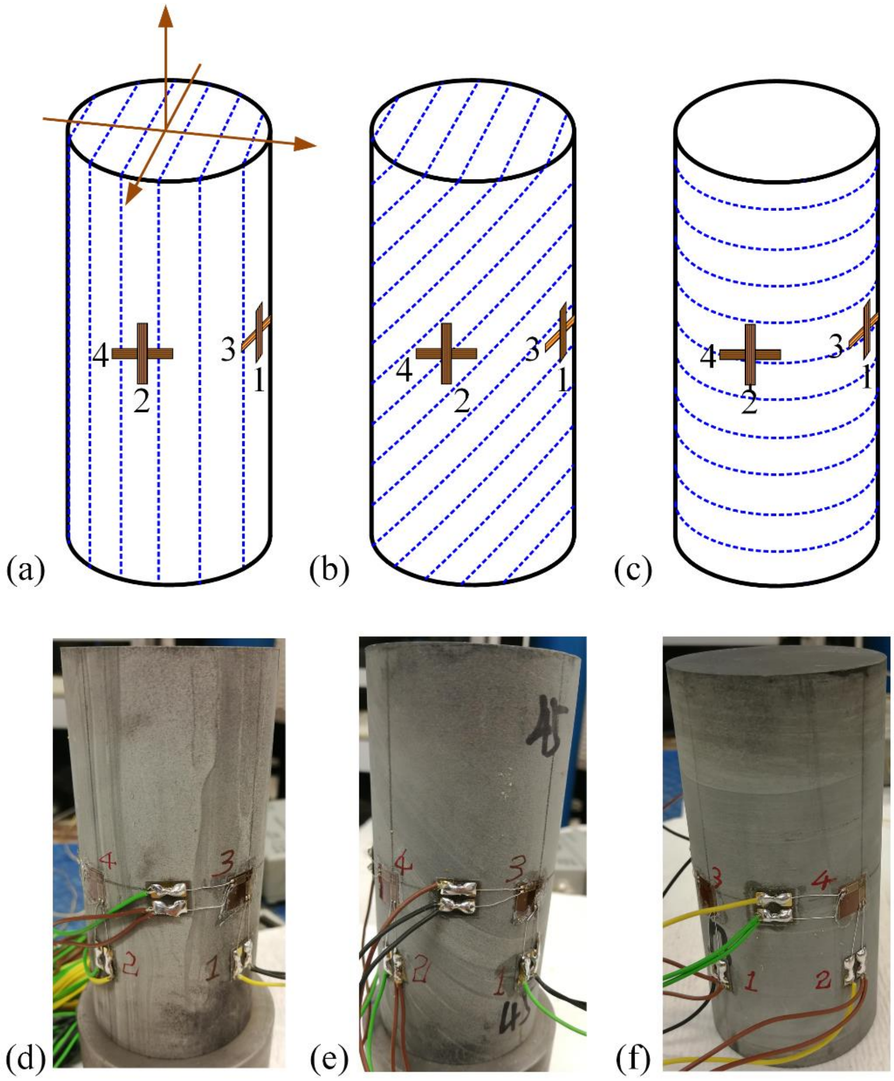

Fig. 3

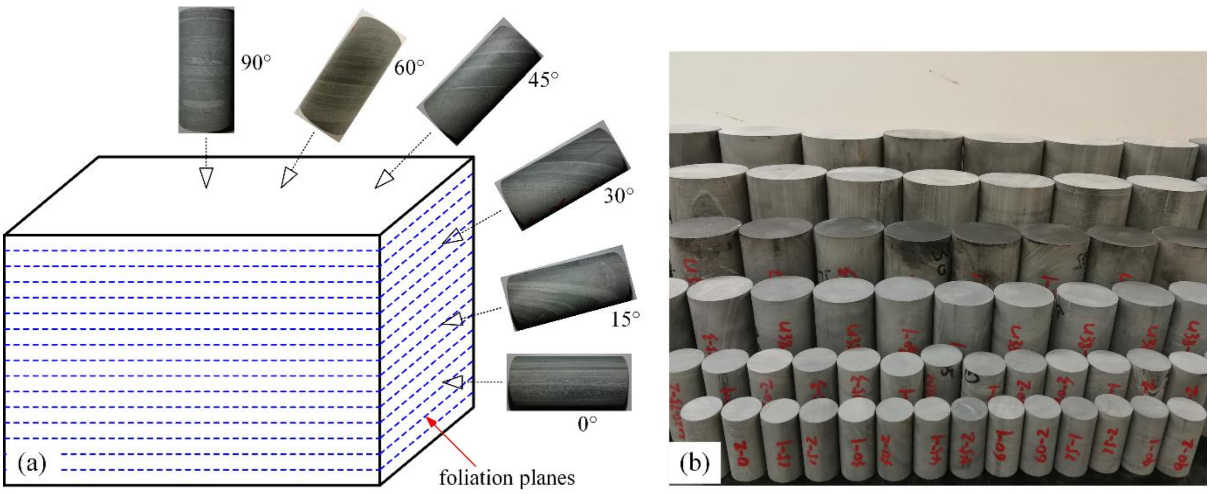

Fig. 4

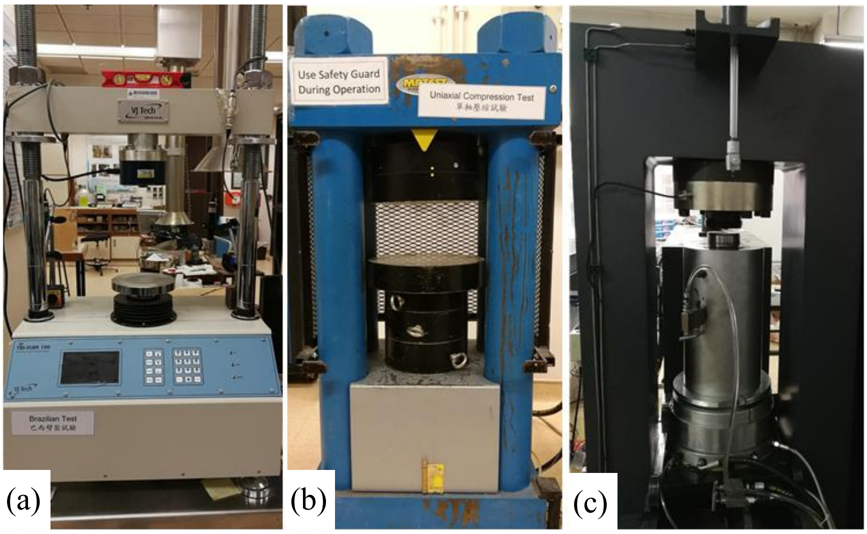

Use Safety Guard
During Operation
Uniaxial Compression Test
Brazilian Test
VJ Tech

(a) (b) (c)

Fig. 5

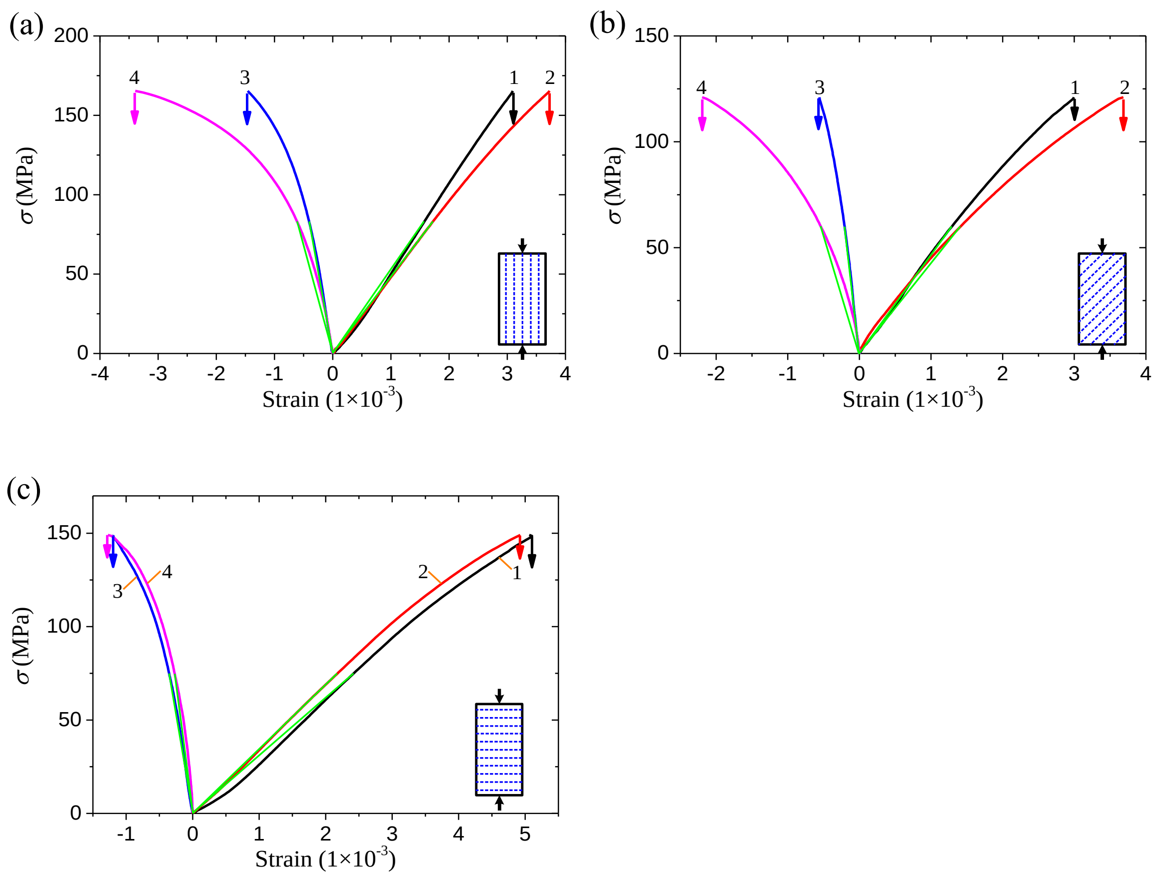
(a)
σ (MPa)
Strain (1×10-3)
1
2
3
4
(b)
σ (MPa)
Strain (1×10-3)
1
2
3
4
(c)
σ (MPa)
Strain (1×10-3)
1
2
3
4

Fig. 6

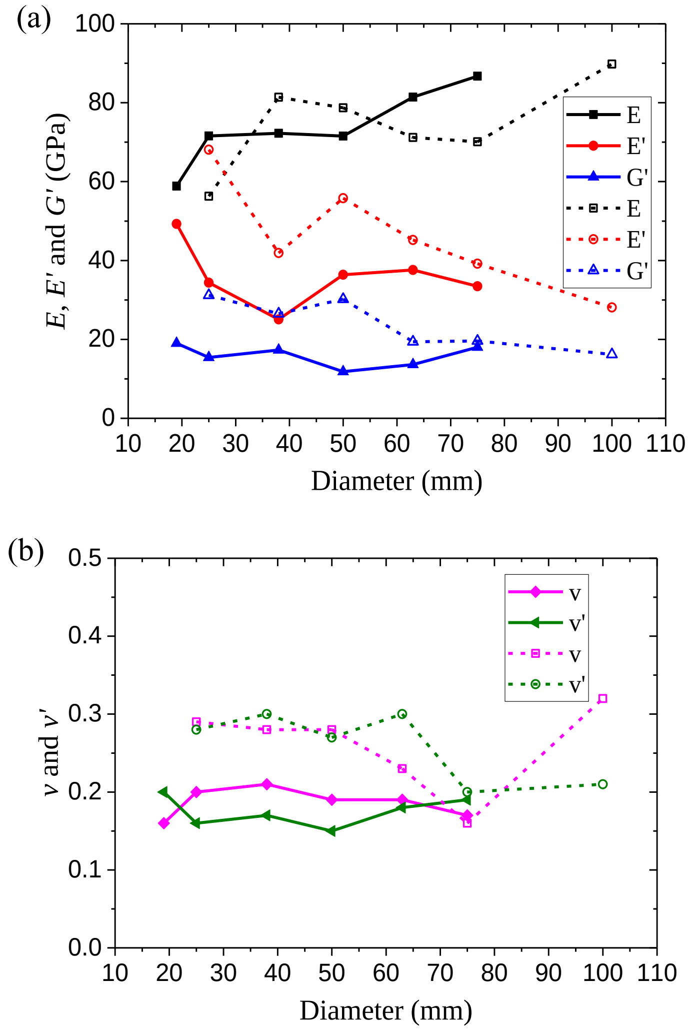

(a)
E, E' and G' (GPa)
0
20
40
60
80
100
10 20 30 40 50 60 70 80 90 100 110
Diameter (mm)
E
E'
G'
E
E'
G'
(b)
v and v'
0.0
0.1
0.2
0.3
0.4
0.5
10 20 30 40 50 60 70 80 90 100 110
Diameter (mm)
v
v'
v
v'

Fig. 7

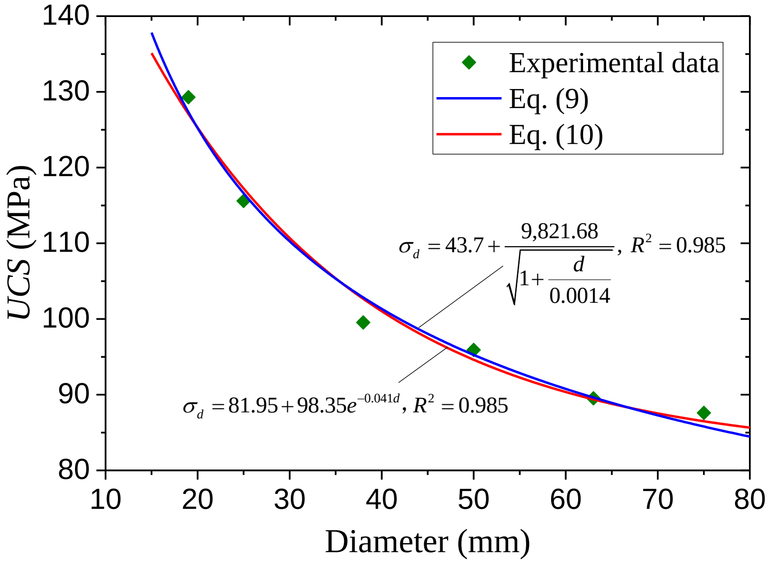

Experimental data
Eq. (9)
Eq. (10)
$\sigma_d = 43.7 + \frac{9,821.68}{\sqrt{1+\frac{d}{0.0014}}}$, $R^2 = 0.985$
$\sigma_d = 81.95 + 98.35e^{-0.041d}$, $R^2 = 0.985$
UCS (MPa)
Diameter (mm)
140
130
120
110
100
90
80
10
20
30
40
50
60
70
80

Fig. 8

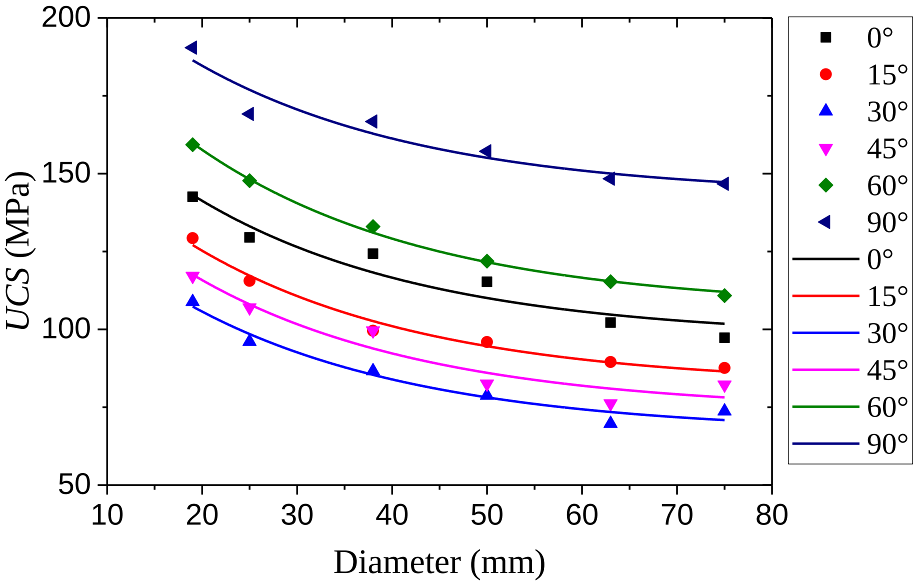
UCS (MPa)
Diameter (mm)
200
150
100
50
10
20
30
40
50
60
70
80
0°
15°
30°
45°
60°
90°
0°
15°
30°
45°
60°
90°

Fig. 9

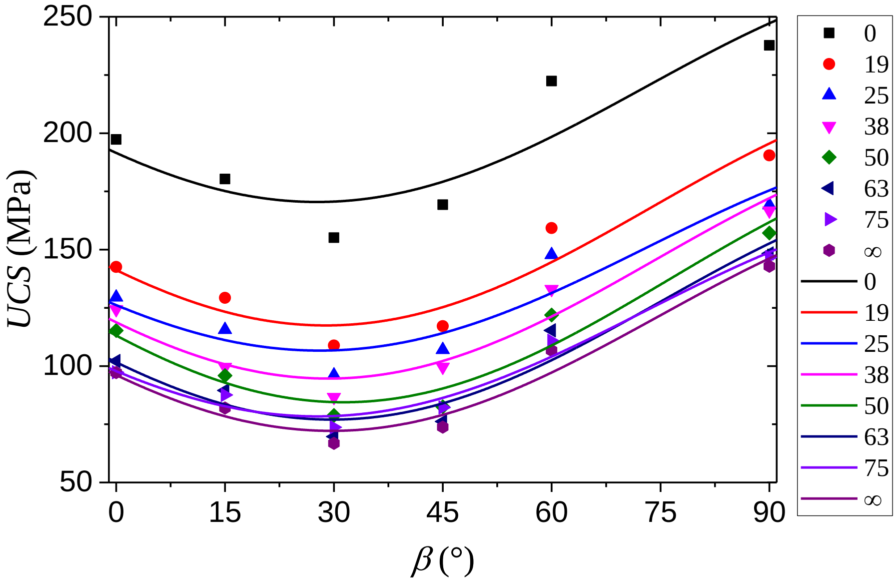

UCS (MPa)
250
200
150
100
50
0
15
30
45
60
75
90
β (°)
0
19
25
38
50
63
75
∞
0
19
25
38
50
63
75
∞

Fig. 10

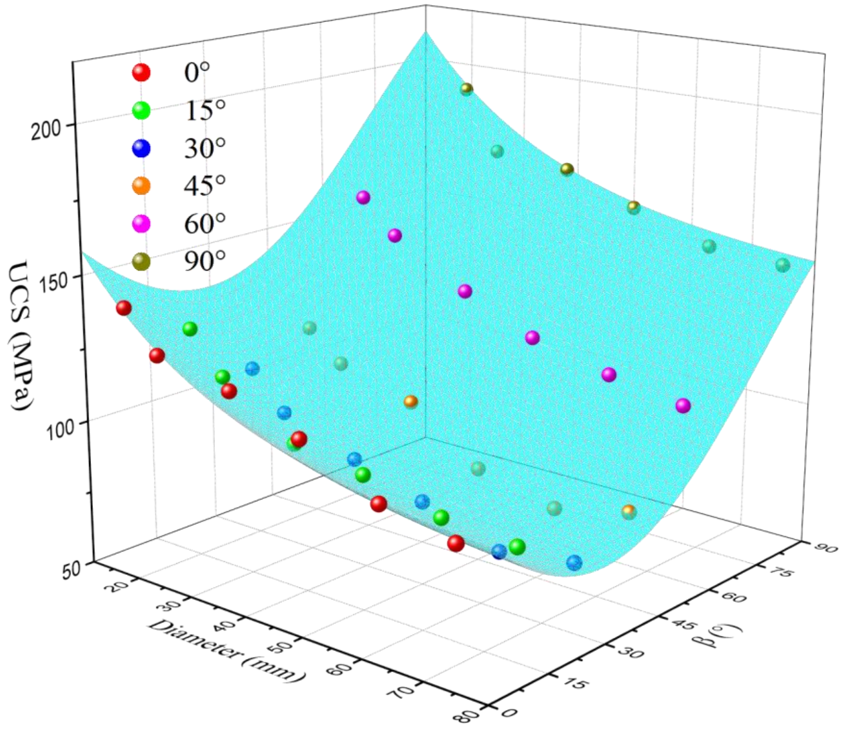
0°
15°
30°
45°
60°
90°
UCS (MPa)
200
150
100
50
20
30
40
50
60
70
80
Diameter (mm)
0
15
30
45
60
75
90
β (°)

Fig. 11

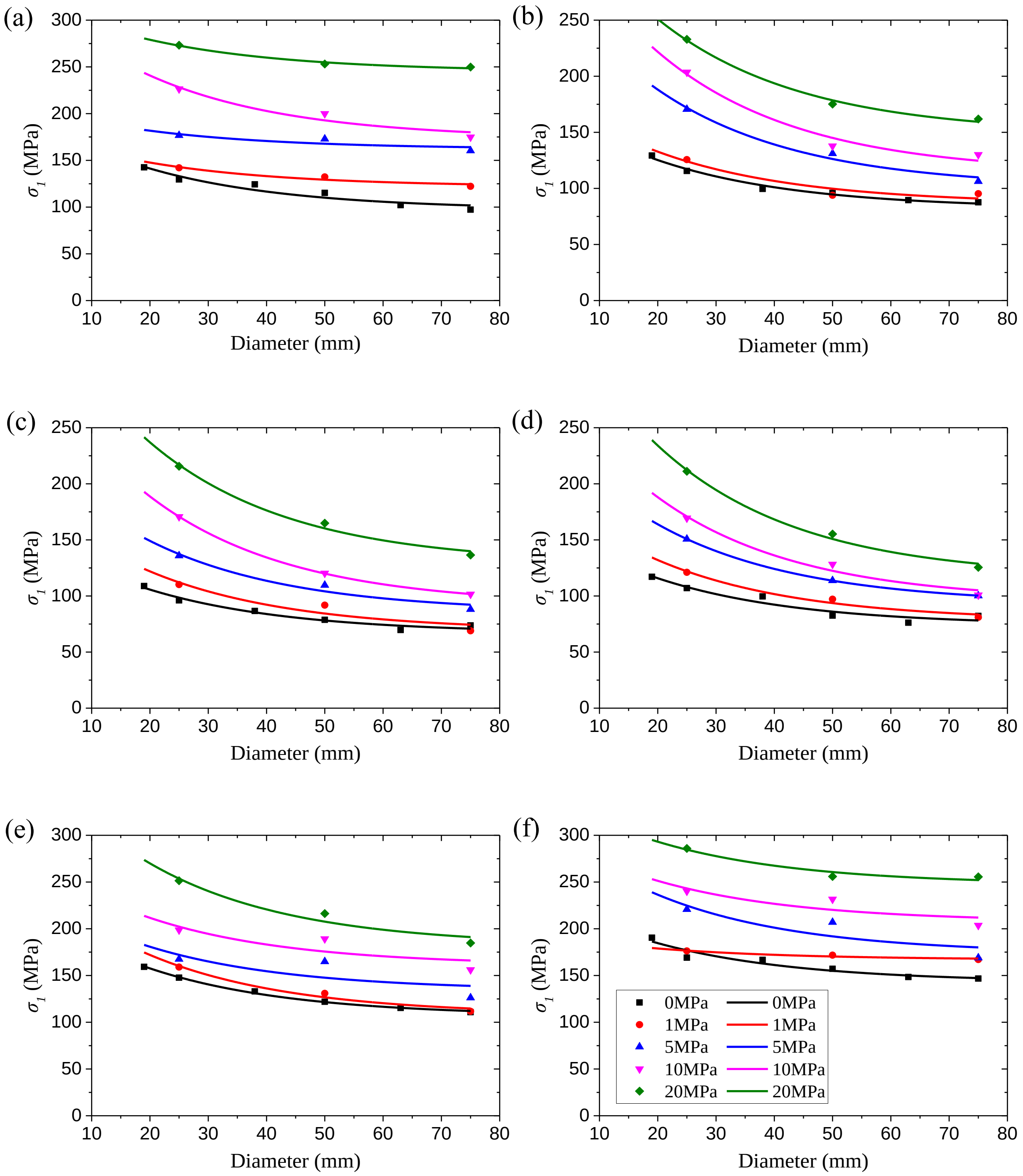

Fig. 12

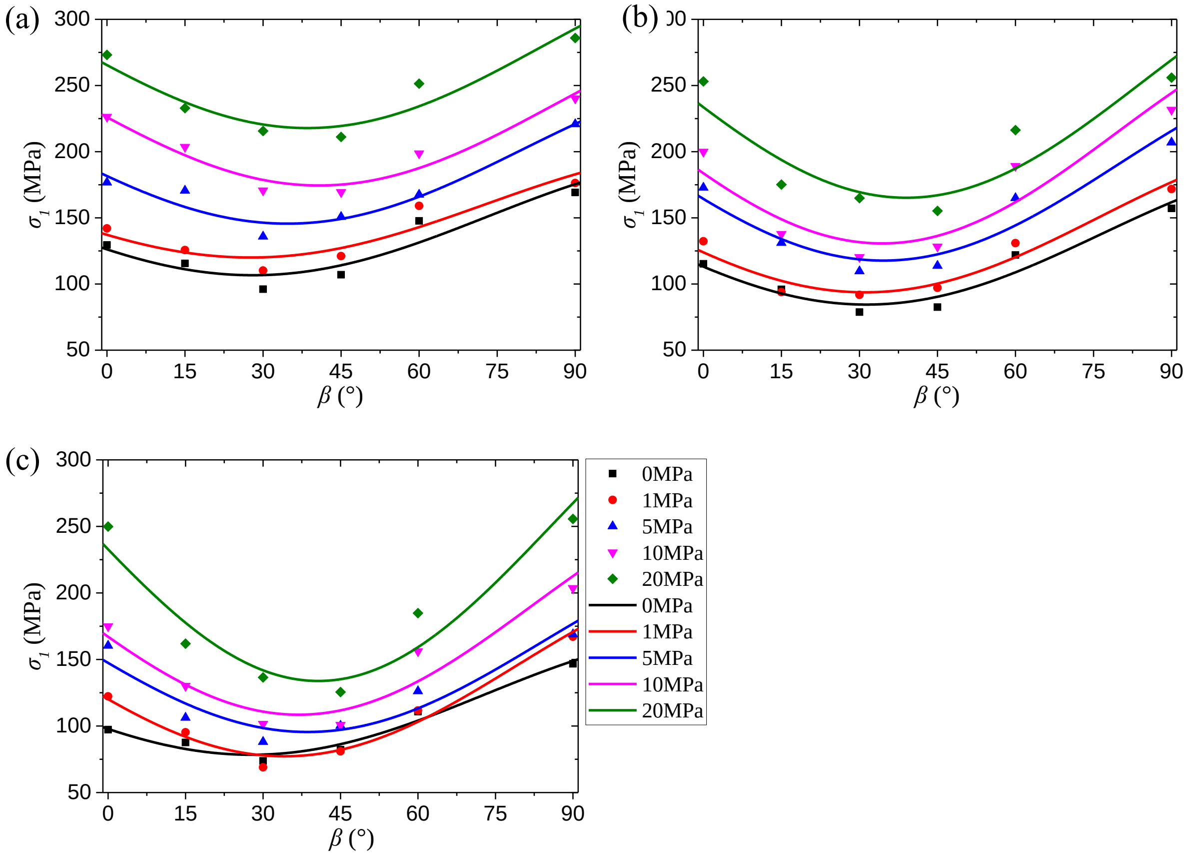
(a)
(b)
(c)
300
250
200
150
100
50
0
15
30
45
60
75
90
σ_1 (MPa)
β (°)
0MPa
1MPa
5MPa
10MPa
20MPa

Fig. 13

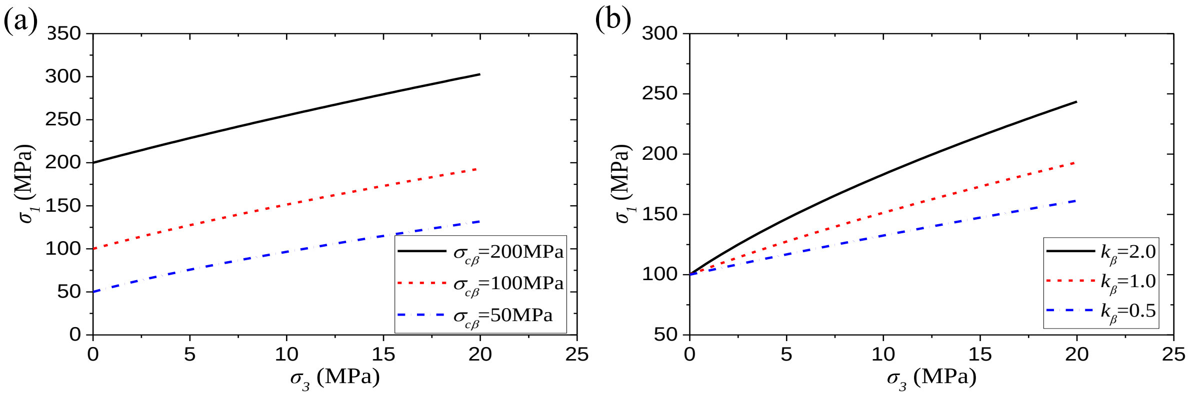
(a)
σ_1 (MPa)
σ_3 (MPa)
$\sigma_{c\beta}$=200MPa
$\sigma_{c\beta}$=100MPa
$\sigma_{c\beta}$=50MPa
0 50 100 150 200 250 300 350
0 5 10 15 20 25
(b)
σ_1 (MPa)
σ_3 (MPa)
k_β=2.0
k_β=1.0
k_β=0.5
50 100 150 200 250 300
0 5 10 15 20 25

Fig. 14

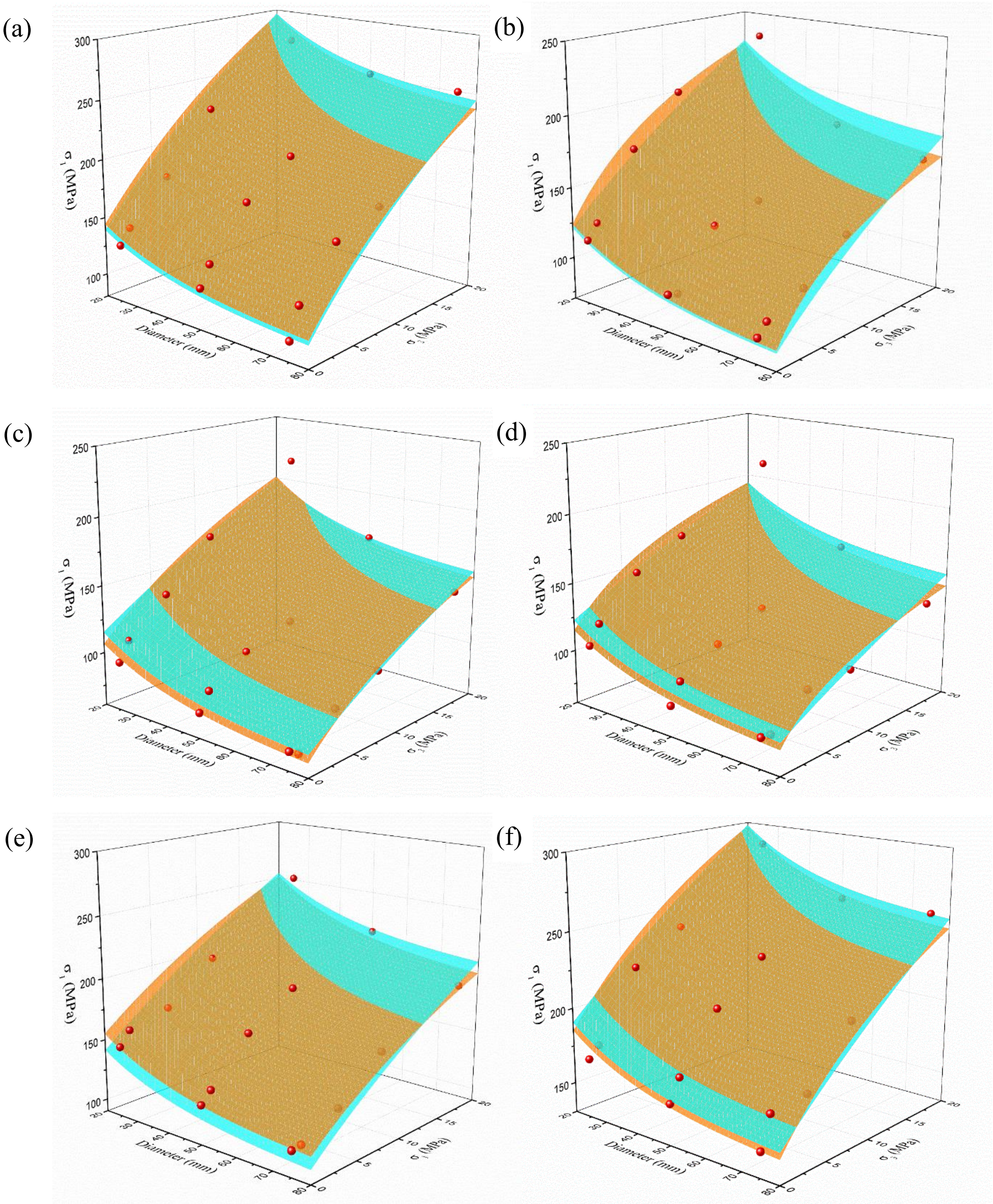

Fig. 15

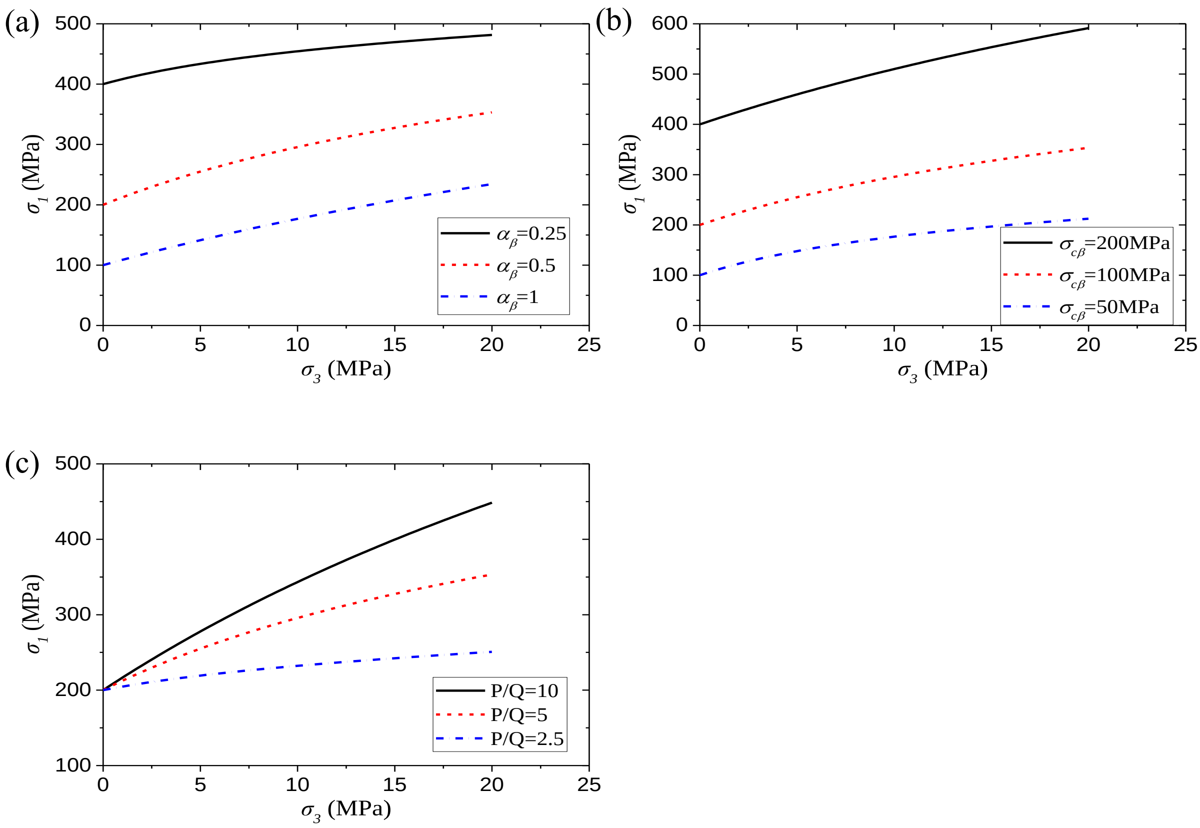
(a)
(b)
(c)
σ_1 (MPa)
σ_3 (MPa)
α_β=0.25
α_β=0.5
α_β=1
$\sigma_{c\beta}$=200MPa
$\sigma_{c\beta}$=100MPa
$\sigma_{c\beta}$=50MPa
P/Q=10
P/Q=5
P/Q=2.5

Fig. 16

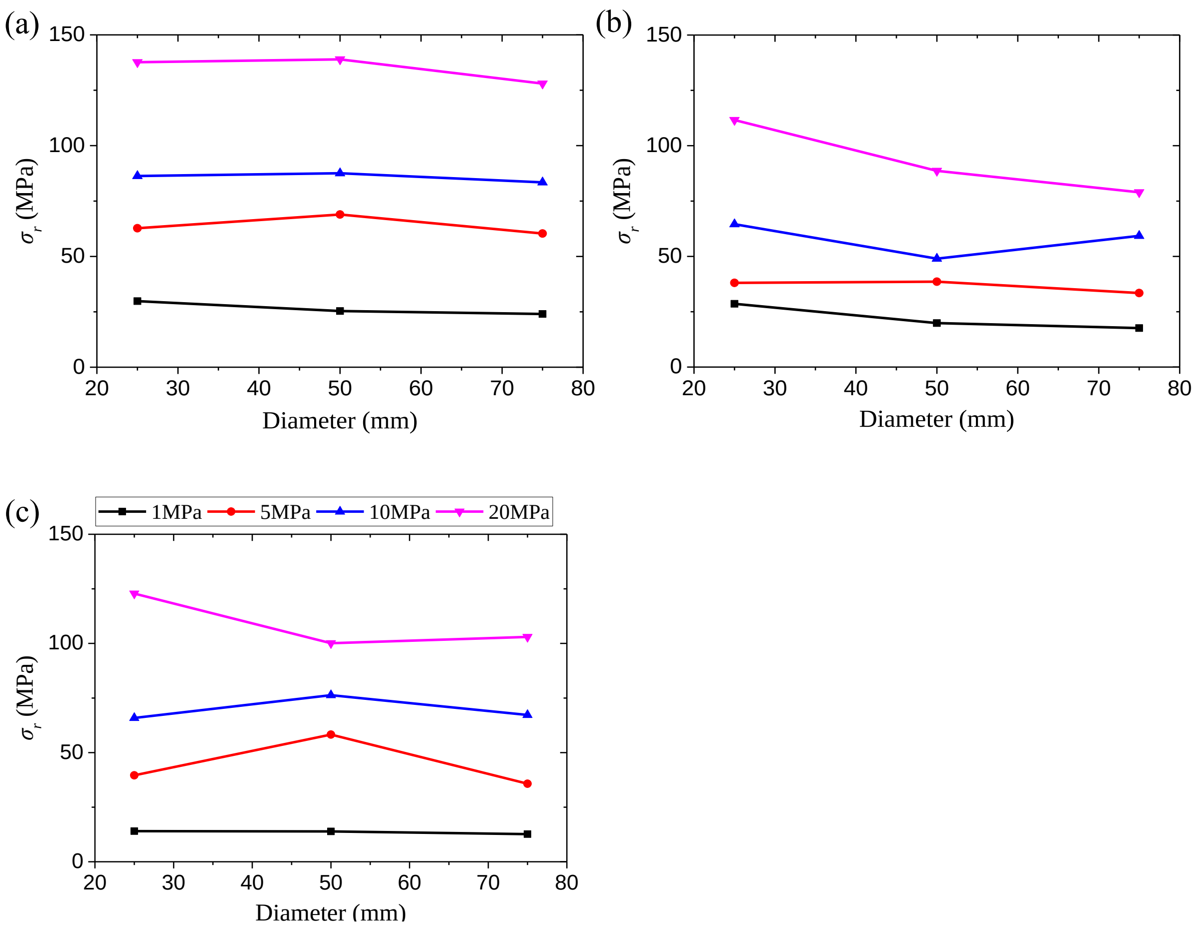

(a)
(b)
(c)
σ_r (MPa)
Diameter (mm)
0
50
100
150
20
30
40
50
60
70
80
1MPa
5MPa
10MPa
20MPa

Fig. 17

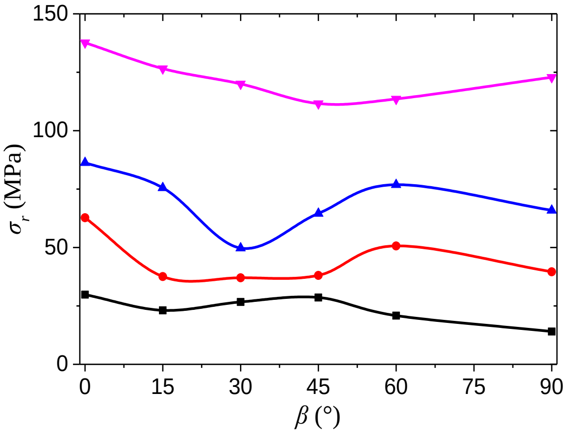

150
100
50
0
σ_r (MPa)
0 15 30 45 60 75 90
β (°)

(a)

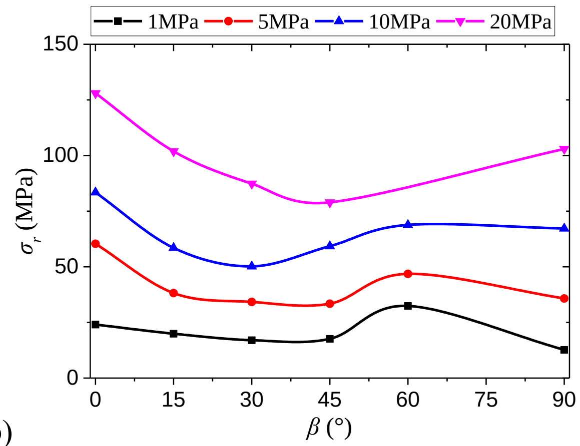

1MPa
5MPa
10MPa
20MPa
150
100
50
0
σ_r (MPa)
0 15 30 45 60 75 90
β (°)

(b)

Fig. 18

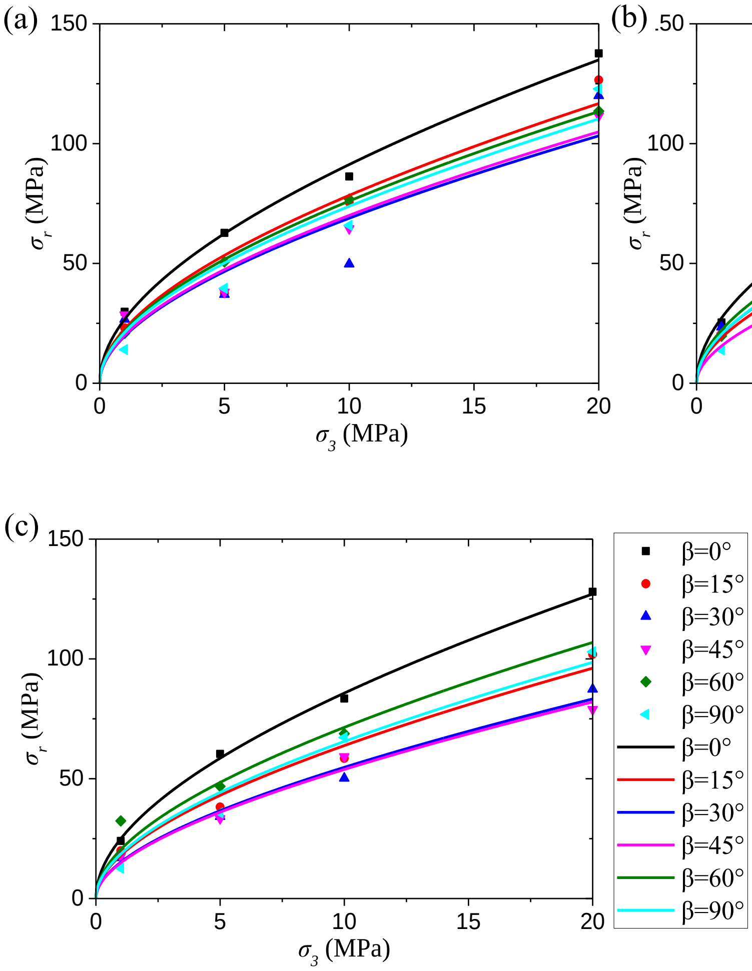
(a)
(b)
(c)
σ_r (MPa)
σ_3 (MPa)
0
50
100
150
0
5
10
15
20
β=0°
β=15°
β=30°
β=45°
β=60°
β=90°

Fig. 19

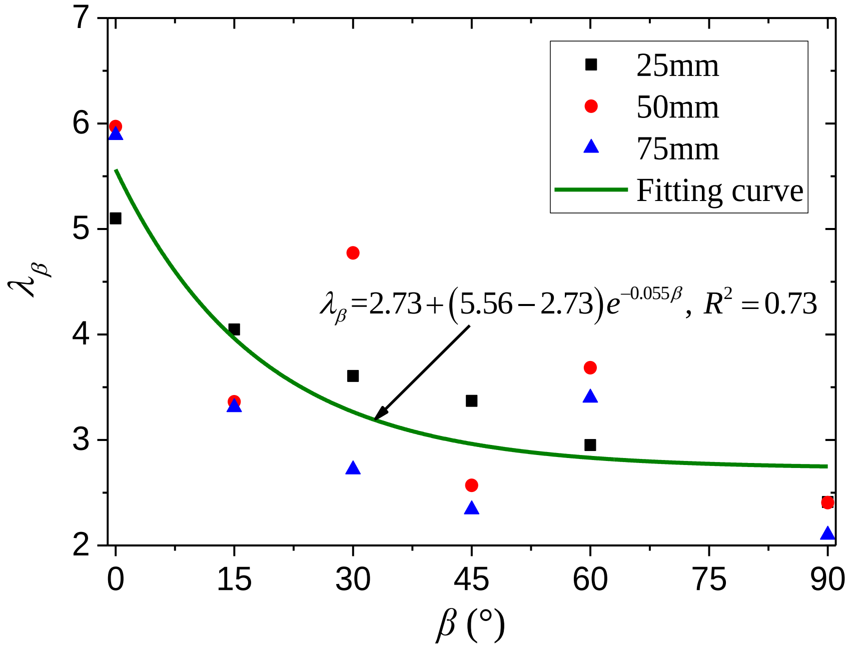
25mm
50mm
75mm
Fitting curve
$\lambda_\beta = 2.73 + (5.56 - 2.73)e^{-0.055\beta}$, $R^2 = 0.73$
λ_β
β (°)
0
15
30
45
60
75
90
2
3
4
5
6
7

Fig. 20

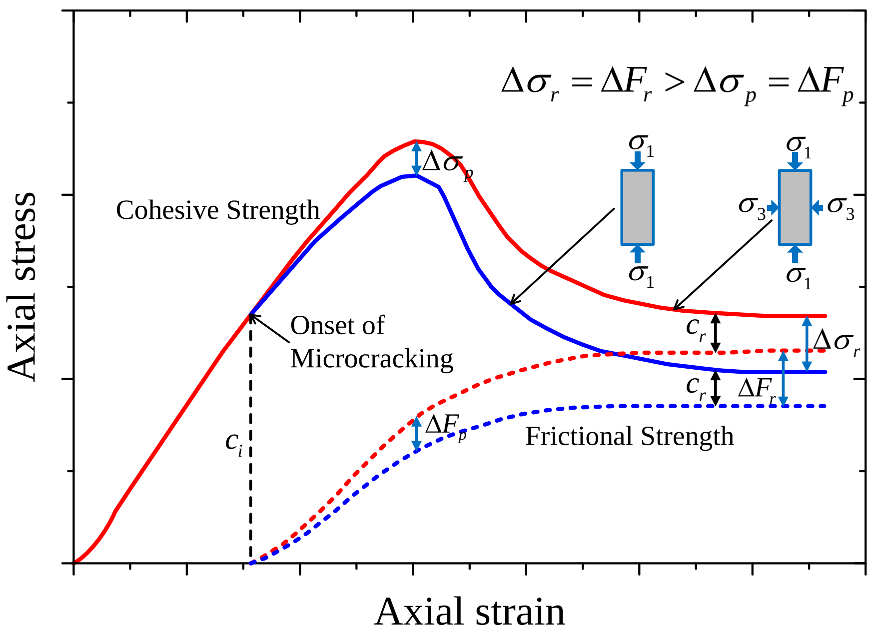
$\Delta\sigma_r = \Delta F_r > \Delta\sigma_p = \Delta F_p$
σ_1
σ_3
Cohesive Strength
$\Delta\sigma_p$
Onset of
Microcracking
c_i
c_r
$\Delta\sigma_r$
ΔF_r
ΔF_p
Frictional Strength
Axial stress
Axial strain

Fig. 21

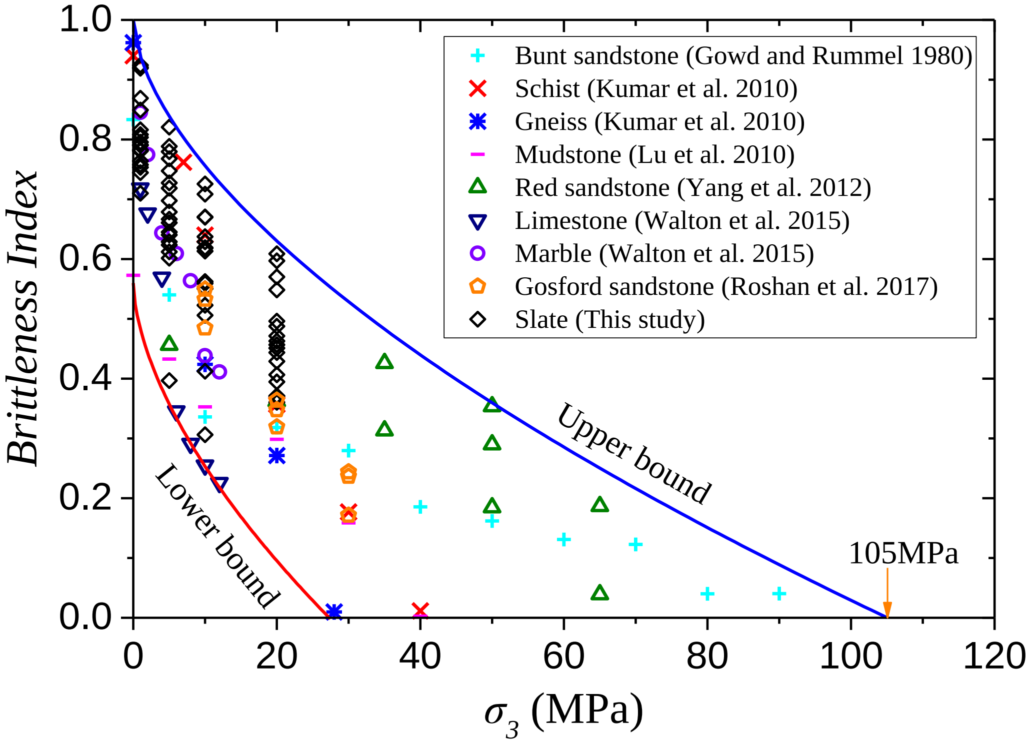

Bunt sandstone (Gowd and Rummel 1980)
Schist (Kumar et al. 2010)
Gneiss (Kumar et al. 2010)
Mudstone (Lu et al. 2010)
Red sandstone (Yang et al. 2012)
Limestone (Walton et al. 2015)
Marble (Walton et al. 2015)
Gosford sandstone (Roshan et al. 2017)
Slate (This study)
Upper bound
Lower bound
105MPa
Brittleness Index
σ_3 (MPa)
1.0
0.8
0.6
0.4
0.2
0.0
0
20
40
60
80
100
120

Fig. 22

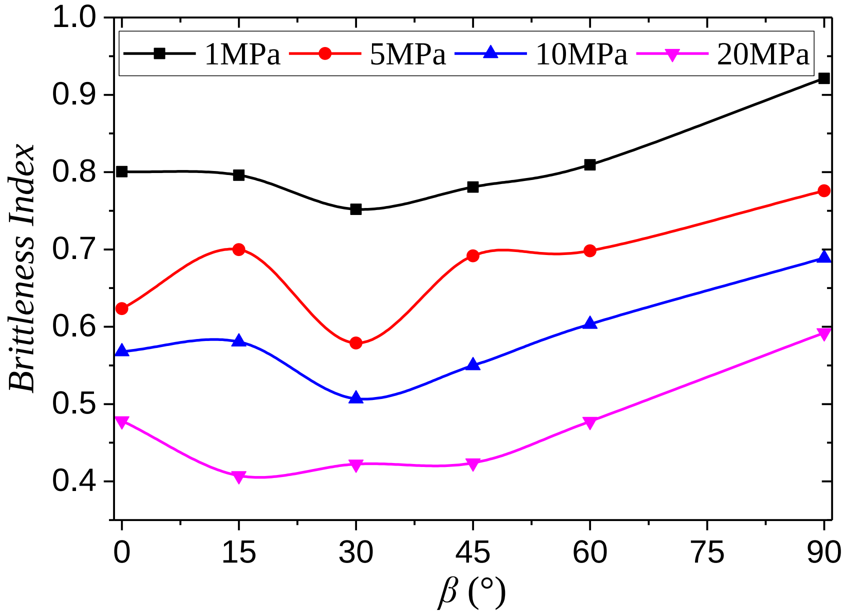
1MPa
5MPa
10MPa
20MPa
Brittleness Index
1.0
0.9
0.8
0.7
0.6
0.5
0.4
0
15
30
45
60
75
90
β (°)

Supplementary material for

Size effect and anisotropy in a transversely isotropic rock under compressive conditions

Kaihui Li (kaihuili_csu@163.com)

School of Resources and Safety Engineering, Central South University, Changsha 410083, China

Introduction

Table S1 and S2 present the compressive strength and triaxial residual strength of slate specimens with different sizes and loading directions at different confining pressures, respectively.

Table S1 Compressive strength of slate specimens with different sizes and loading directions at different confining pressures

Diameter (mm)	β =0°			β =15°			β =30°		
	σ_3 (MPa)	σ_1 (MPa)	SD* (MPa)	σ_3 (MPa)	σ_1 (MPa)	SD (MPa)	σ_3 (MPa)	σ_1 (MPa)	SD (MPa)
19	0	142.58	11.40	0	129.29	19.18	0	108.83	7.29
25	0	129.53	2.92	0	115.59	12.59	0	96.07	11.79
	1	142.06	18.55	1	125.67	—	1	110.15	22.38
	5	176.75	2.39	5	170.60	3.06	5	135.89	49.27
	10	226.33	12.39	10	203.58	7.20	10	170.67	—
	20	273.19	—	20	232.91	9.42	20	215.67	1.31
38	0	124.31	6.70	0	99.55	10.12	0	86.62	27.99
50	0	115.25	0.75	0	95.91	7.45	0	78.77	7.31
	1	132.31	17.44	1	93.88	15.32	1	91.82	3.67
	5	172.88	45.31	5	131.12	0.63	5	109.68	4.35
	10	199.92	20.98	10	137.74	1.11	10	120.29	2.27
	20	253.09	6.14	20	175.15	2.69	20	164.86	21.74
63	0	102.16	7.03	0	89.52	1.50	0	69.72	10.44
75	0	97.29	22.15	0	87.59	14.34	0	73.72	19.59
	1	122.25	0.90	1	95.32	14.68	1	68.93	0.36
	5	160.37	13.67	5	106.25	9.21	5	88.16	20.04
	10	174.85	1.02	10	130.06	—	10	101.53	3.58
	20	249.85	—	20	161.89	—	20	136.53	—
Diameter (mm)	β =45°			β =60°			β =90°		
	σ_3 (MPa)	σ_1 (MPa)	SD (MPa)	σ_3 (MPa)	σ_1 (MPa)	SD (MPa)	σ_3 (MPa)	σ_1 (MPa)	SD (MPa)
19	0	117.12	6.33	0	159.29	11.39	0	190.46	7.66
25	0	107.01	7.00	0	147.74	33.61	0	169.14	10.64

	1	121.07	7.41	1	159.06	—	1	176.32	10.69
	5	150.73	7.89	5	167.56	16.36	5	220.80	1.75
	10	169.37	2.80	10	198.69	16.91	10	240.16	6.67
	20	211.13	37.74	20	251.38	—	20	285.91	—
38	0	99.60	12.51	0	133.01	6.66	0	166.71	16.61
50	0	82.51	3.31	0	121.92	6.78	0	157.17	7.40
	1	97.13	3.26	1	130.87	7.63	1	171.74	2.69
	5	113.76	2.31	5	164.94	3.95	5	207.01	0.16
	10	128.21	22.12	10	189.19	0.21	10	231.60	3.69
	20	155.26	8.96	20	216.28	6.17	20	255.96	2.69
63	0	76.21	28.43	0	115.31	14.34	0	148.38	9.05
75	0	82.21	1.39	0	110.84	27.30	0	146.72	0.21
	1	80.94	0.88	1	111.65	18.48	1	167.10	—
	5	100.23	0.07	5	126.21	14.61	5	168.97	—
	10	100.83	2.19	10	156.10	1.04	10	203.64	—
	20	125.51	0.19	20	184.79	—	20	255.59	—

* SD stands for one standard deviation.

Table S2 Triaxial residual strength of slate specimens with different sizes and loading directions at different confining pressures

Diameter (mm)	β =0°			β =15°			β =30°		
	σ_3 (MPa)	σ_r (MPa)	SD* (MPa)	σ_3 (MPa)	σ_r (MPa)	SD (MPa)	σ_3 (MPa)	σ_r (MPa)	SD (MPa)
25	1	29.81	0.59	1	23.10	—	1	26.69	3.92
	5	62.73	1.00	5	37.58	1.88	5	37.02	1.13
	10	86.28	1.26	10	75.52	8.39	10	49.74	—
	20	137.65	—	20	126.55	3.72	20	119.99	7.07
50	1	25.36	1.70	1	20.57	2.93	1	23.44	3.46
	5	68.90	—	5	42.12	0.41	5	66.15	—
	10	87.54	—	10	60.31	0.05	10	83.45	2.95
	20	138.92	0.06	20	106.02	3.42	20	88.56	1.27
75	1	24.03	1.93	1	19.92	4.07	1	17.01	2.50
	5	60.34	3.97	5	38.20	7.24	5	34.19	1.98
	10	83.44	4.99	10	58.48	0.55	10	50.17	4.13
	20	128.03	—	20	101.91		20	87.33	—
Diameter (mm)	β =45°			β =60°			β =90°		
	σ_3 (MPa)	σ_r (MPa)	SD (MPa)	σ_3 (MPa)	σ_r (MPa)	SD (MPa)	σ_3 (MPa)	σ_r (MPa)	SD (MPa)
25	1	28.58	2.35	1	20.84	—	1	14.01	1.63
	5	38.05	5.17	5	50.68	—	5	39.60	2.00
	10	64.55	6.24	10	76.85	3.78	10	65.87	1.12
	20	111.59	—	20	113.55	—	20	122.84	—
50	1	19.84	0.74	1	19.73	0.25	1	13.90	—
	5	38.58	6.80	5	38.27	—	5	58.26	—
	10	48.95	2.29	10	68.60	0.25	10	76.30	—
	20	88.67	4.48	20	128.34	4.67	20	100.10	—

75	1	17.61	1.42	1	32.37	1.81	1	12.67	—
	5	33.42	6.57	5	46.82	—	5	35.76	—
	10	59.27	4.38	10	68.79	7.63	10	67.22	—
	20	78.94	0.31	20	—	—	20	102.98	—

* SD stands for one standard deviation.